Chapter 4

Intrinsic Defects in ZnO: Synthesized by Various Techniques

CHAPTER-4
Intrinsic Defects in ZnO: Synthesised by Various Techniques

ZnO being a well known optoelectronic semiconductor, investigation related to defects is very promising. In this chapter, we have attempted to detect the defects using various spectroscopic techniques in ZnO nanoparticles synthesised through different chemical routes. In Section 4.1, microstructure through XRD and SEM, vibrational modes through Raman, cationic defects through PAS and optical properties of ZnO synthesised through coprecipitation technique are discussed. Section 4.2 and 4.3 elaborate the similar studies in ZnO synthesised through sol-gel and combustion routes. Finally in the last Section 4.4 we have summarised the results obtained from all these techniques.

4.1 Coprecipitation

ZnO nanoparticles are synthesised at different *p*H of precipitation such as 5.5, 7, 9, 10, 11.5 and 13.0 and dried at 80 ^{o}C and 250 ^{o}C. The dried ZnO powder is subjected to various characterisations to explore its properties.

4.1.1 Microstructural Studies by XRD and SEM

XRD patterns of the ZnO powder dried at 80 ^{o}C for 24 h, are shown in Fig. 4.1. At lower *p*H (5.5 and 7.0), in addition to minor ZnO phase (JCPDS file no. 36-1451), phase of zinc hydroxide nitrate hydrate ($Zn_5(OH)_8(NO_3)_2(H_2O)_2$ - JCPDS file no. 72-0627 and 24-1460) is found as a major phase. XRD patterns of the samples synthesised at *p*H 9.0 and 10.0 show the wurtzite phase of ZnO. All observed peaks match well with the diffraction peaks corresponding to (100), (002), (101), (102), (110), and (103) planes of wurtzite structure of ZnO (JCPDS file no. 36-1451). With increasing *p*H to 11.5 and 13.0, the appearance of intermediate secondary phase of wulfingite ε-$Zn(OH)_2$ (JCPDS file no. 89-0138) is observed along with the ZnO phase. These samples are dried at 250 ^{o}C for 5 h, synthesised at different *p*H. The XRD patterns of dried ZnO powders are shown in Fig. 4.2. No characteristic

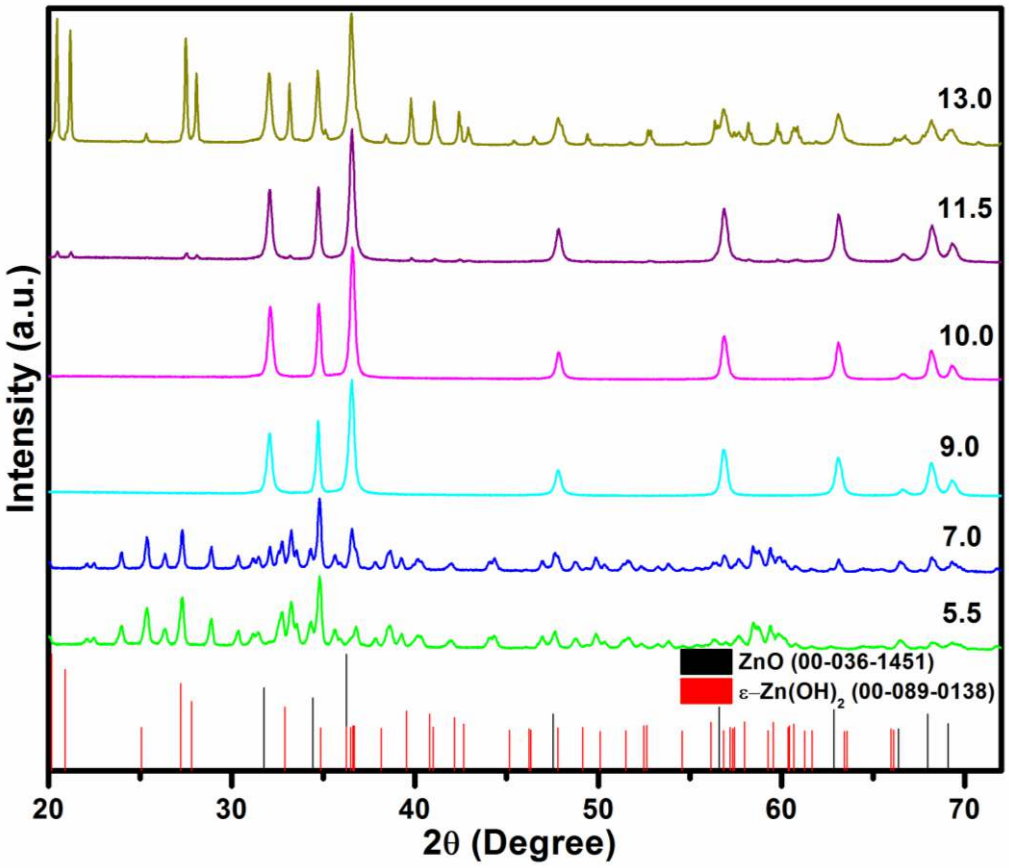

Figure 4.1: The XRD patterns of the ZnO powder synthesised at different *p*H (5.5, 7, 9, 10, 11.5 and 13.0), dried at 80 ^{o}C for 24 h**.**

peaks of any intermediate or secondary phase related to $Zn_5(OH)_8(NO_3)_2(H_2O)_2$ or ε-$Zn(OH)_2$ could be detected from the diffraction pattern. At 250 ^{o}C, calcination the $Zn_5(OH)_8(NO_3)_2(H_2O)_2$ and $Zn(OH)_2$ completely transforms into crystalline ZnO. By using the Scherrer formula [Scherrer *et al*. (1918)], the crystallite size of ZnO particles synthesised at *p*H 5.5, 7, 9, 10, 11.5 and 13.0 are found to be 63.2, 76.5, 46.9, 35.3 and 36.6, 36.7 nm, respectively.

At a *p*H 7 and below, presence of $Zn_5(OH)_8(NO_3)_2(H_2O)_2$ phase is due to partial neutralisation of $Zn(NO_3)_3$ solution with NaOH base solution. In between *p*H 7 and *p*H 10, compleate neutralisation of $Zn(NO_3)_3$ takes place, resulting into the pure phase of ZnO. As ZnO is an amphoteric compound [Degen *et al*. (2000)], therefore, at higher *p*H (above 11.5 pH) it dissolves in concentrated alkali (NaOH) solution and follows the crystallisation of $Zn(OH)_2$, resulting into the coexistence of both ZnO and $Zn(OH)_2$ phase at

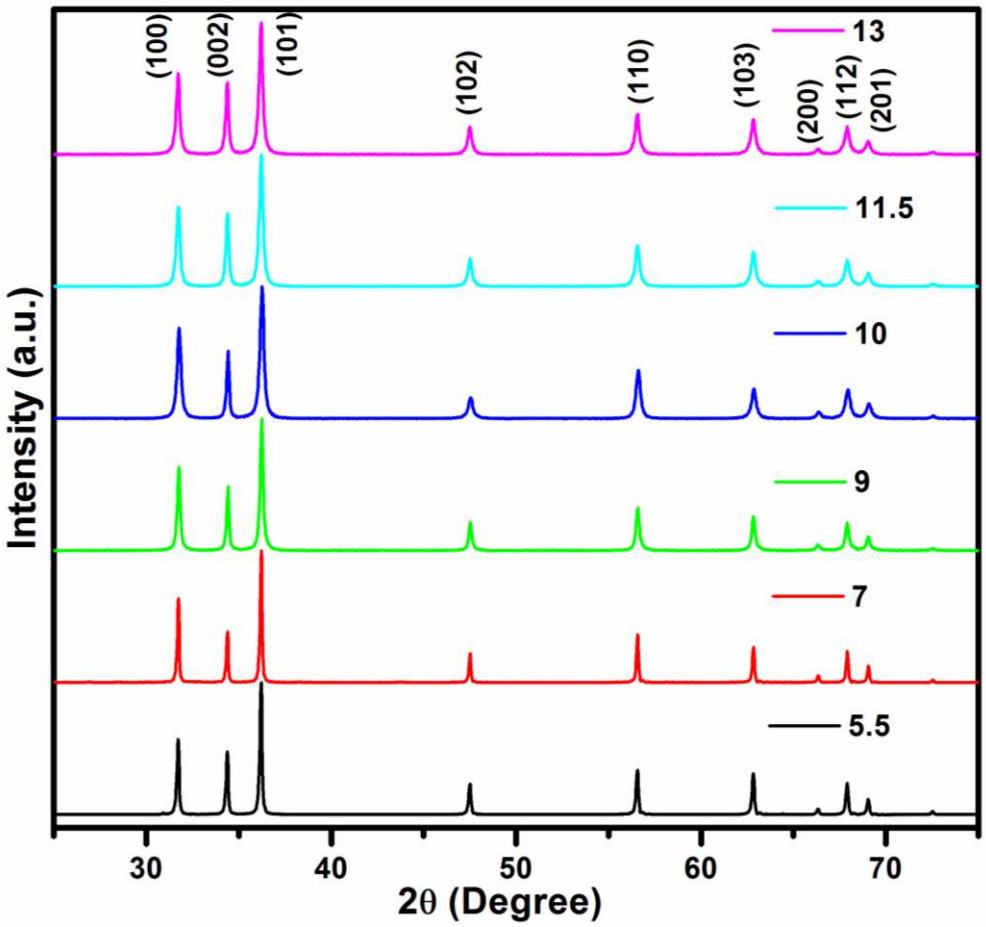

Figure 4.2: The XRD patterns of the ZnO powder synthesised at different *p*H (5.5, 7, 9, 10, 11.5 and 13.0), dried at 250 ^{o}C for 5 h**.**

*p*H 11.5 and *p*H 13 samples dried at 80 ^{o}C. $Zn_5(OH)_8(NO_3)_2(H_2O)_2$ is thermodynamically very unstable at and above 160 ^{o}C it rapidly transforms into ZnO by dissolution [Music *et al*. (2007)]. Similarly, zinc hydroxide is stable upto 110 °C, but decomposes above that temperature to a series of less hydrated phases, with associated loss of mass, until zinc oxide is formed mostly at about 190 °C [Moezzi *et al*. (2013)]. Therefore, in the present case, drying the samples synthesised at different *p*Hs at 250 ^{o}C results into pure phase of ZnO. Audebrand *et al*. (1998) have synthesised ZnO at 170 ^{o}C using $Zn(NO_3)_3$ precursor which is the lowest temperature so for. However, we have been able to reduce the temperature to 80 ^{o}C by tuning the *p*H inbetween 9 and 10 using same $Zn(NO_3)_3$ as a precursor. The isoelectric point (IEP) of ZnO is found in the literature, ranging from *p*H 8.7 to 10.3, which is the most stable/favourable range for synthesis of ZnO. Our *p*H range is well within the *p*H range (9-10

*p*H) [Parks *et al*. (1965); Reed *et al*. (1986)]. Therefore, we reveal that at 80 ^{o}C and between *p*H 9-10, pure ZnO can be synthesised using $Zn(NO_3)_3$ precursor in a easy and cost effective way.

Morphologies of the products characterised through FE-SEM, synthesised at different *p*H (5.5, 7, 9, 10, 11.5 and 13.0), are shown in Fig 4.3. We observe two dimensional micron sized plates at *p*H 5.5, mixed triangular and hexagonal rods at *p*H 7, hexagonal rods at *p*H 9 and 10, needle-like crystals at *p*H 11.5 and hierarchical structures at *p*H of 13. It is clear from the micrographs that not only size, the shape of ZnO nanoparticles greatly depends on the *p*H of precipitation. Sequential growth of 2D plates to triangular, hexagonal rods, needle shaped crystals and finally flower like morphology is quite interesting result obtained in case of ZnO, just by increasing *p*H of precipitate. At lowest *p*H 5.5 and 7, the major phase is $Zn_5(OH)_8(NO_3)_2(H_2O)_2$ compound as observed from XRD. It has been reported that the (100) plane of $Zn_5(OH)_8(NO_3)_2(H_2O)_2$ compound consists of a high density of Zn-O atoms which have a pseudohexagonal arrangement on the projection and generally forms like plate from the above layered compound that supports our result [Music *et al*. (2007); Wahab *et al*. (2009)]. At *p*H 7, in addition to plates, like morphology we also observe triangular and hexagonal rods. Increasing the *p*H from 7 to 11.5, rods and needles are observed. It has been shown that, formation of rods, needles or wires are due to the growth along [0001] direction of ZnO. The mechanism behind the growth of different morphology observed in our case can be described by stacking of a number of tetrahedrally coordinated O^{2-} and Zn^{2+} ions either side by side or along the c-axis. Sequence of growth of various morphologies are depicted in Fig 4.4. It has been reported in literature that neutral and alkaline solution of Zn^{2+} ion hydrolyses to form a series of species of $Zn(OH)_n^{(2\ -\ n)}$ (n = 1–4) [Degen *et al*. (2000)]. The hydrolysis products of $Zn(OH)_2$ and $Zn(OH)^{2-}_4$ have tetrahedral geometry. Their coordination numbers and the Zn-O distance are very similar to those of ZnO [Lippincott *et al*. (1952)]. The growth unit of the ZnO crystal thus has tetrahedral coordination.

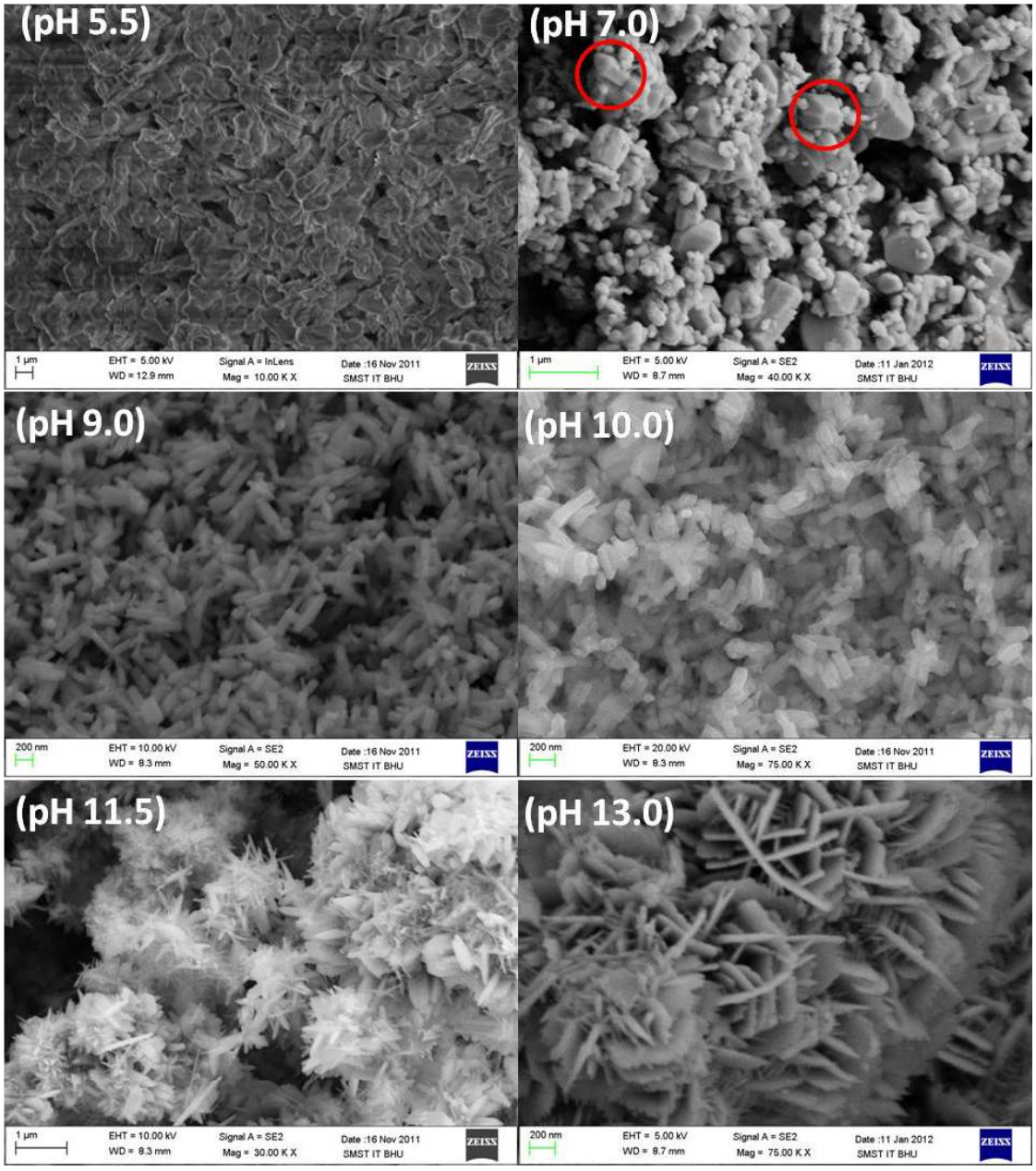

Figure 4.3: The SEM image of the ZnO powder synthesised at different *p*H (5.5, 7, 9, 10, 11.5 and 13.0) of precipitation and dried at 80 ^{o}C for 5 h**.**

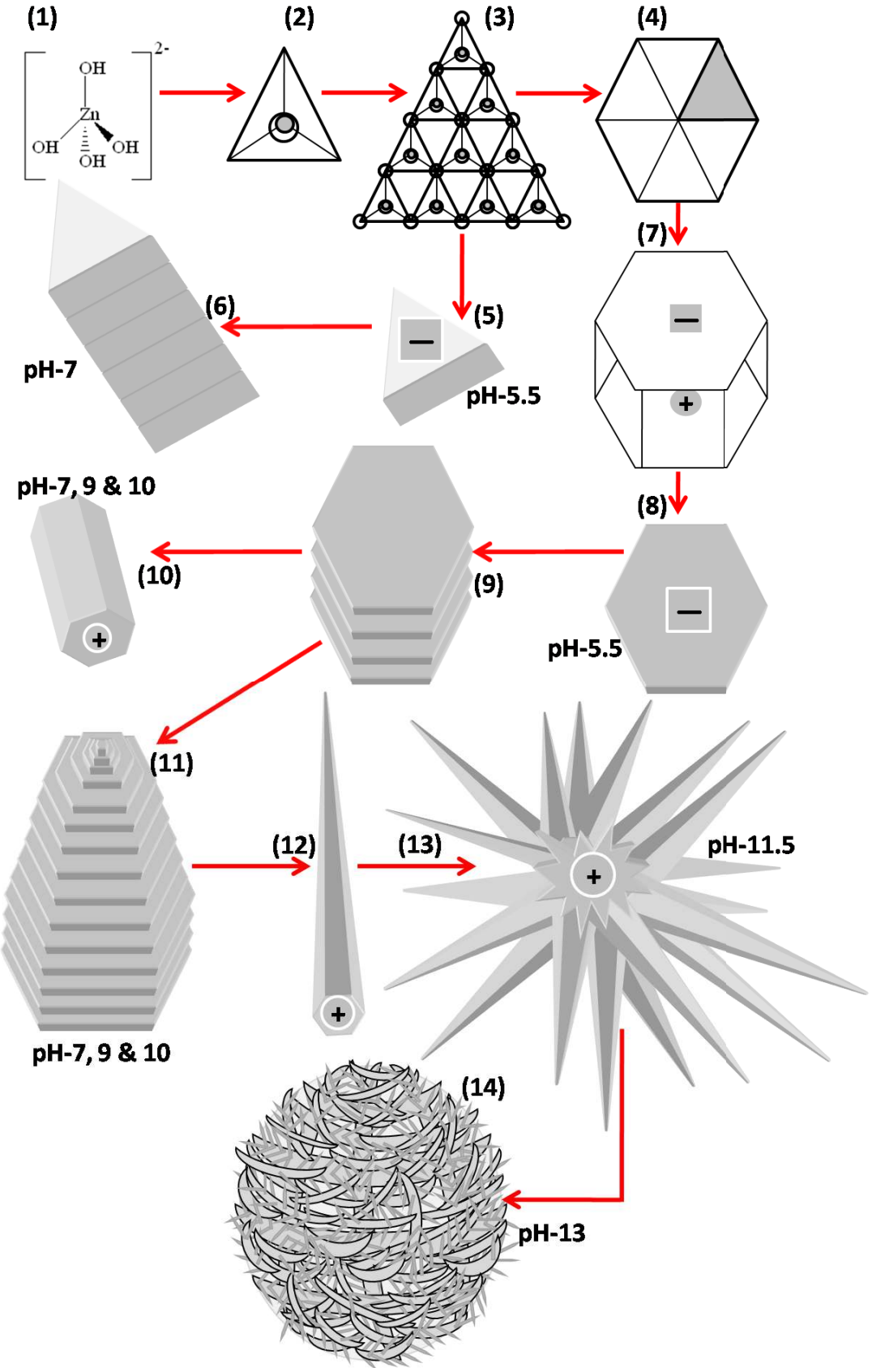

Figure 4.4: Schematic diagram of the growth of ZnO under coprecipitation route with varying the *p*H (5.5, 7, 9, 10, 11.5 and 13.0) of solution during synthesis.

The tetrahedrally coordinated O^{2-} and Zn^{2+} ions represented in step-1 as shown in Fig 4.4 forms the building block or basis for the growth of various morphologies of ZnO. The basis is represented as a tetragonal shape, shown in step-2. The stacking of this basis side by side (perpendicular to *c*-axis) or alternatively along the *c*-axis results into either triangular and/or hexagonal rod. The stacking of this basis side by side in triangular or hexagonal shapes has shown in step 3 and 4, respectively. As the surface is polar in nature, the stacking occurs alternatively along the *c*-axis in addition to side by side perpendicular to c-axis that results into triangular and hexagonal bar as shown in step 5 and 7, respectively. At neutral *p*H sample i.e. 7, stacking the triangular and hexagonal bars alternatively along the *c*-axis, we thus observe triangular and hexagonal rod shape shown as step 6 and step 8, 9 and 10. Increasing *p*H to 10, the growth of rods occurs and we observe rods of about ~70 nm diameter and ~180 nm length throughout the samples. The mechanism for growth of the hexagonal rod involves step 8, 9 and 10, where the rods are formed by stacking the hexagonal bars alternatively along the *c*-axis consistent with expected layer-by-layer growth mechanisms [Li *et al*. (1999); Sun *et al*. (2012); Han *et al*. (2009); Shen *et al*. (2006); Nicholas *et al*. (2012); Krishnan *et al*. (2009); Joo *et al*. (2013)]. SEM image of *p*H 11.5 samples demonstrate very dense bunches of flowers. A close view indicates that a single flower is composed of large number of needle-like petals arising from the center of the flower. The lengths of needles are 100-300 nm. The tapered needle- or obelisk-like ends of high-aspect-ratio rod are formed by multiple steps of stacking of hexagonal layers with decreasing surface area, as shown in step 11, 12 and 13. In literature, we found that the end planes of the nanorods are smooth hexagons that correspond to the ±(0001) crystal plane of ZnO [Shen *et al*. (2006)]. In our case, we also presume that all ZnO products have the same [0001] growth direction though they have quite different morphologies. It is easy for wurtzite ZnO to grow into anisotropic one-dimensional structure [Shen *et al*. (2006)]. The flower like structure is observed in sample synthesised at *p*H 13, which is different from that of the sample synthesised at *p*H 11.5. The magnified view of

the sample made at *p*H 13 indicates that the micro sized flowers exhibit a hierarchical structure. Interestingly, the flower-like 3D structures are assembled by a large number of nanosheets and small needles. The nanosheets intersect with each other, which results in a net-like structure and the needles are grown on these sheets are shown in step 14 of Fig. 4.4. The above results demonstrate that the growth environment has a significant influence on the final morphology of ZnO crystals.

4.1.2 Detection of Vibrational Modes Using Raman spectroscopy

As Raman scattering is fast, sensitive and non-destructive technique to study crystal structure, structural disorder in lattice and defects in micro-/nanostructures, we have carried out room temperature Raman measurement of ZnO samples synthesised at different *p*H. The hexagonal ZnO crystal has a wurtzite structure of space group C_{6v}^4 with two formula units per primitive cell that gives rise to six Raman active modes at the Γ- point of the Brillouin zone. The modes can be represented as in (4.1),

$$\Gamma_{opt} = A_1 + 2B_1 + E_1 + 2E_2 \quad (4.1)$$

The polar modes A_1 and E_1 vibrations split into longitudinal (LO) and transverse optical (TO) phonon modes in presence of long-range coulomb field. A non polar E_2 mode is Raman-active whereas B_1 mode is Raman-inactive [Duan *et al*. (2010)]. The Raman spectra of ZnO powder synthesised at different *p*H (5.5, 7.0, 9.0, 10.0, 11.5 and 13.0) and dried at 80 ^oC are shown in Fig. 4.5. The observed Raman modes are compared with the reported vibrational modes [Manjon *et al*. (2005); Cusco *et al*. (2007)]. In the lower range of the Raman spectrum 200-800 cm^{-1}, for samples synthesized at 5.5 and *p*H 7.0, we observe extra Raman peaks marked as '*' in addition to first order Raman modes of ZnO such as E_1(TO), E_2(high), second order phonon mode, $2E_2$ as well as few multi phonon modes (MP). These additional peaks may arise due to intermediate phase of $Zn_5(OH)_8(NO_3)_2(H_2O)_2$ and the presence of residual nitrate precursor in the sample. One additional mode around 531 cm^{-1} is also observed in the spectra. The first order Raman modes A_1(TO), E_1(TO), E_2(high), A_1(LO), E_1(LO) and second order phonon mode, $2E_2$ are completely

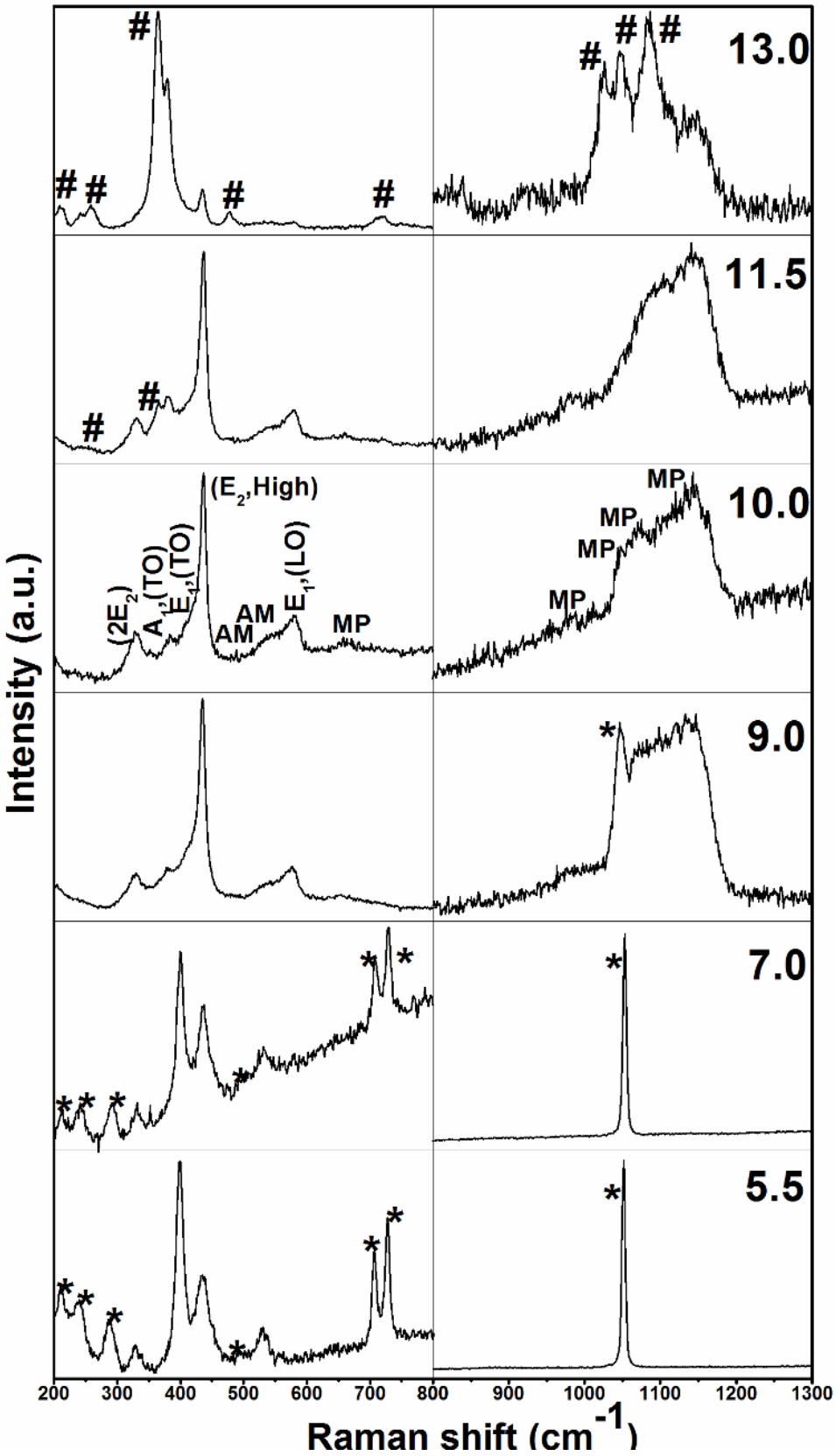

Figure 4.5: The Raman spectrum of the ZnO powder synthesised at different *p*H (5.5, 7, 9, 10, 11.5 and 13.0) and dried at 80 ^{o}C for 24 h**.**

matched in samples synthesised at *p*H 9.0 and *p*H 10.0. Two additional modes (AM) appear at 515 and 531 cm^{-1} for samples synthesised at *p*H 9.0 and 10.0. Increasing the *p*H from 10 to 11.5, in addition to regular peaks of ZnO, low intensed peaks are also observed. These Raman peaks are represented as '#' and become dominant in sample synthesised at *p*H 13 (Fig. 4.5). The extra Raman peaks could be due to the secondary phase of wulfingite ε-$Zn(OH)_2$ as detected from XRD [Music *et al*. (2007)]. Besides the first order and second order phonon modes, a few additional modes (AM) appear at 515 and 531 cm^{-1} in our samples. Similar additional modes have been found in ZnO doped with Ni and Mn at ~524 and 670 cm^{-1} respectively by Wang *et al*. (2003). Other dopants like Sb, Ga and Fe also show additional modes at 511, 531, 644 and 720 cm^{-1} [Bundesmann *et al*. (2003)]. These modes have been attributed to intrinsic host-lattice defects related to doping. Manjon *et al*. (2005) have reported that most of the additional Raman modes observed in doped ZnO samples correspond to the silent modes of ZnO. Serrano *et al*. (2004) have estimated the silent modes theoretically by *ab initio* calculation of the lattice dynamics which are B_1(low), $2B_2$(low), B_1(high), TA+B_1(high) and B_1(low)+B_1(high) are observed at 261, 520, 552, 650 and 810 cm^{-1}, respectively. $2B_2$(low) and B_1(high) modes are in agreement with the additional modes (AM) as observed by us.

In the higher wave number range starting from 800-1300 cm^{-1}, we observe sharp Raman peak at 1053 cm^{-1} in sample synthesised at *p*H 5.5, 7 and *p*H 9. It has been reported as symmetric stretching (ν_1) of NO_3^- ion [Liu *et al*. (2013); Peleg *et al*. (1972); Chang *et al*. (1973)]. The peaks at 708 and 728 cm^{-1} are responsible for in-plane deformation or bending (ν_4) of NO_3^- ion. The unperturbed NO_3^- has D_{3h} symmetry and gives rise to symmetric stretching (ν_1), out-of-plane deformation (ν_2), asymmetric stretching (ν_3) and in-plane deformation or bending (ν_4) modes. The ν_3 and ν_4 modes are both Raman and IR active whereas the ν_1 is Raman active and ν_2 is IR active. At higher *p*H 9 to 11.5, we observe a broad band from 950 to 1200 cm^{-1} with few sharp features. This broad band is made up with several multiphonon (MP) Raman modes of

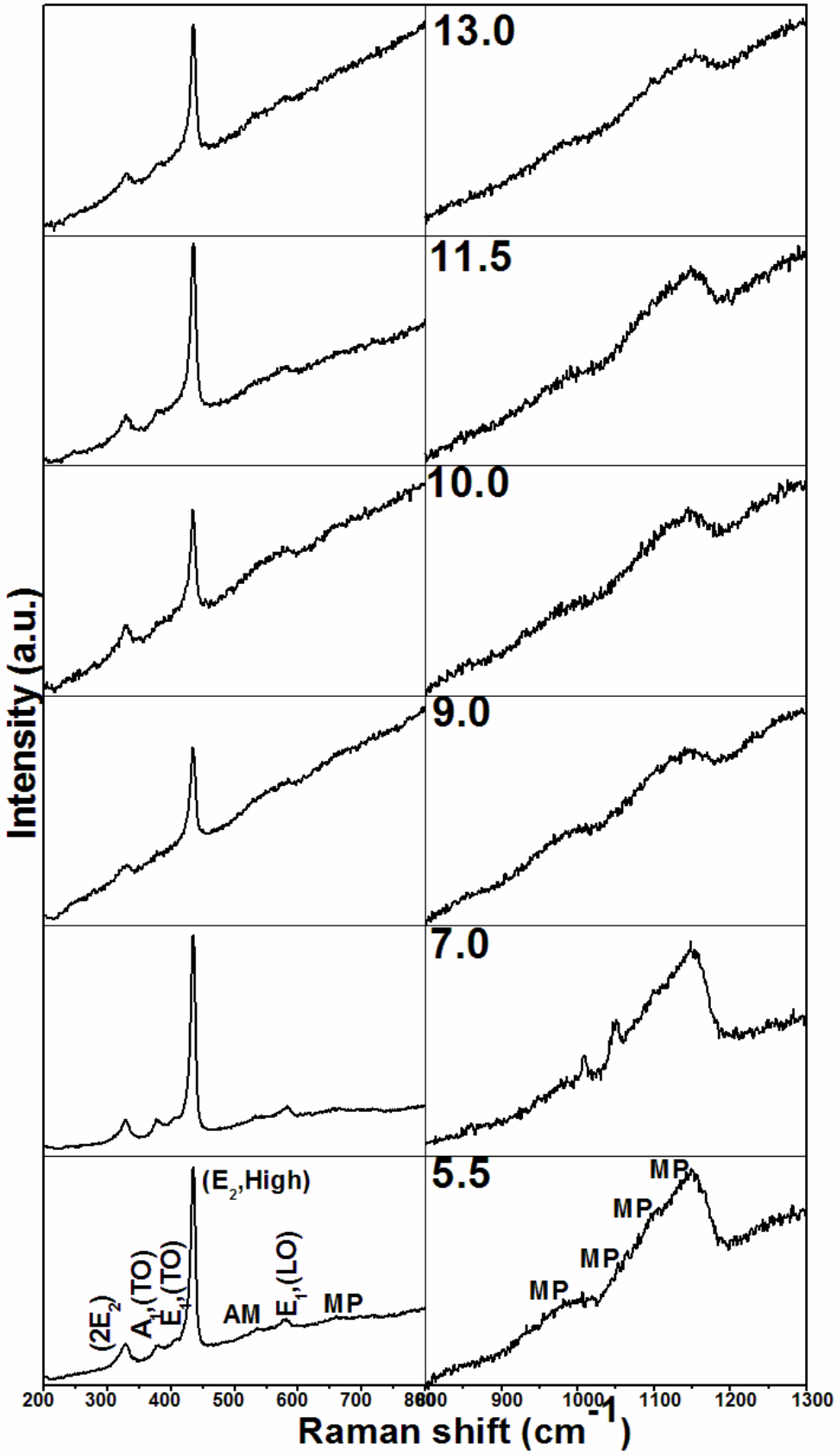

Figure 4.6: The Raman spectrum of the ZnO powder synthesised at different *p*Hs (5.5, 7, 9, 10, 11.5 and 13.0) and dried at 250 ^{o}C for 5 h**.**

ZnO (Fig. 4.5) [Cusco *et al*. (2007)]. In case of *p*H 13, the broad band is made up of the multiphonon Raman modes of ZnO as well as due to the secondary phase of wulfingite ε-$Zn(OH)_2$. The Raman spectrum of ZnO powder synthesised at different *p*Hs and dried at 250 ^oC for 5 h are shown in Fig. 4.6. The Raman spectroscopy of the all ZnO samples dried at 80 °C exhibits Raman scattering peaks only; without any luminescent background. However, for all the samples dried at 250 ^oC possess very strong luminescent backgrounds. The Raman modes of all samples matched well with the ZnO and no characteristic peaks of any intermediate or secondary phase is detected.

4.1.3 Optical Properties Using PL Spectroscopy

Photoluminescence spectra obtained at room temperature for ZnO, synthesised at different *p*Hs and dried at 80 and 250 ^oC, are shown in Fig. 4.7 (a-b). It is clear from the Fig. 4.7 (a) that on excitation with 355 nm, two bands appear in the spectra for all samples except the sample synthesised at *p*H 5.5. The first one is very sharp and intense whereas the second one is broad. The sharp and intense band is due to near band edge (NBE) emission in UV region and the other broad band in visible region is due to defect related deep band emission (DBE) [Liu *et al*. (2010); Alvi *et al*. (2013)]. The former one has been widely regarded as recombination through free excitons and the latter is possibly due to intrinsic defects related emission [Liu *et al*. (2010)]. After drying at 250 ^oC, the DBE band gets suppressed and the NBE band becomes narrower and intense, as shown in Fig 4.7 (b). Very weak band of DBE is observed only for samples made at *p*H 11.5 and 13. It is generally assumed that the crystal quality of ZnO is strongly related to the stability of the NBE emission and the intensity ratio of NBE emission to DBE. Despite several studies, the exact mechanism of carrier recombination processes for NBE and DBE in ZnO nanostructures is still the subject of considerable debates. Various investigations led to different conclusions, and there was no agreement about the origin of these emissions. It has been reported that the excitonic features of the UV emission is associated with free-exciton (FX), donor-bound exciton (D°X), LO-phonon replicas of FX, and LO-phonon replicas of D°X [Yakimova

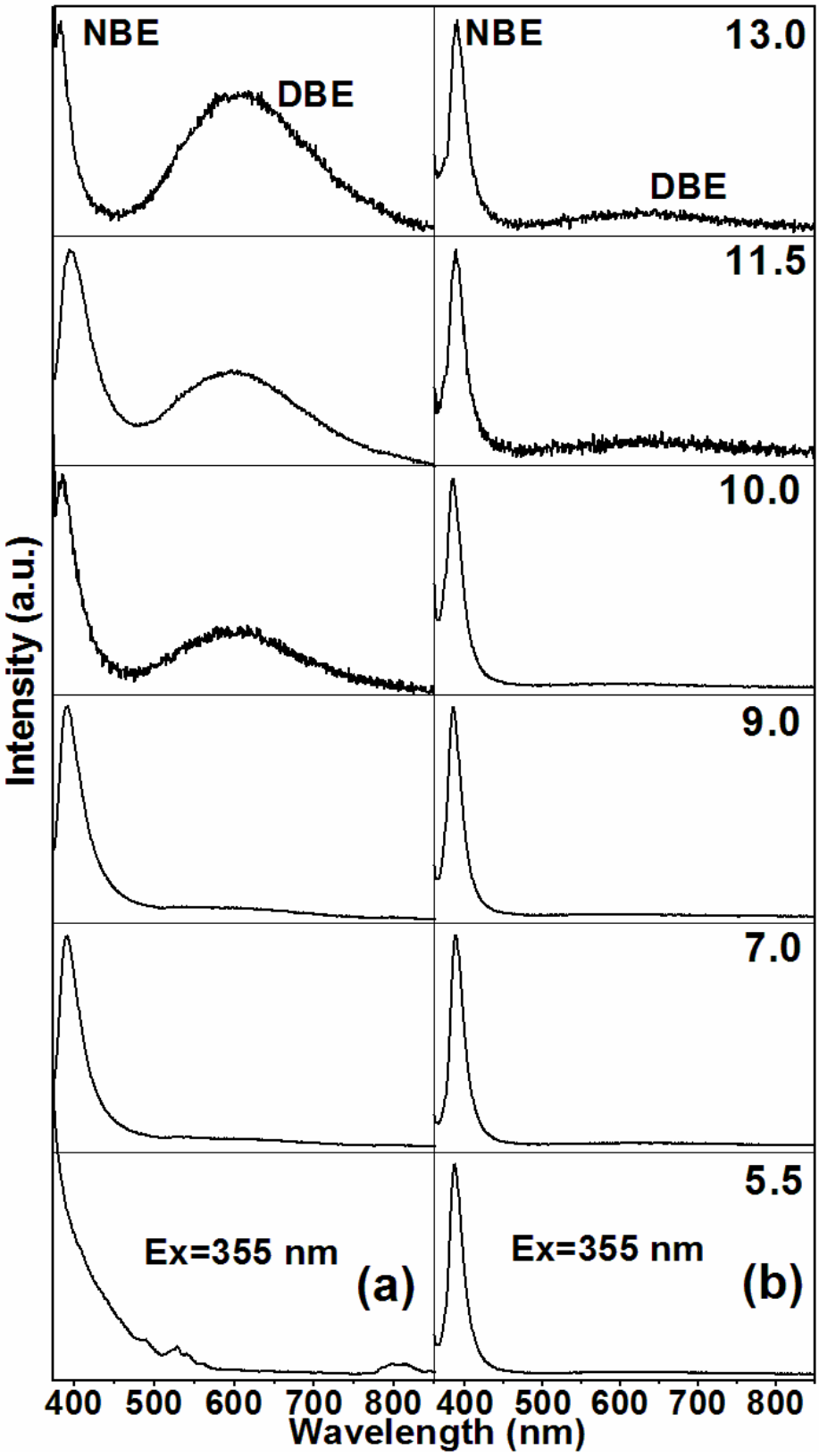

Figure 4.7: The PL spectrum obtained by using the excitation wavelength 355 nm for the ZnO powder synthesised at different *p*H (5.5, 7, 9, 10, 11.5 and 13.0) **(a)** dried at 80 ^{o}C for 24 h, **(b)** dried at 250 ^{o}C for 5 h**.**

et al. (2006); Meyer *et al*. (2004); Chen *et al*. (2009)]. In fact, the visible broad band (DBE) is also reported due to the mixture of blue, green, and yellow emissions. It has been reported by Ke *et al*. (2010) that optical transition occurs in green (2.32 eV), green-yellow (2.21 eV) and yellow-orange (2.07 eV) zones. While green emission is due to Zn vacancies, green-yellow emission is likely due to O vacancies and yellow-orange emission may be caused by O interstitials.

To study the change in DBE band with *p*H, we normalised the NBE emission peak intensity instead of the absolute PL intensity. We observe the gradual increase in DBE band with increasing *p*H for samples dried at 80 °C samples. The DBE covers the visible range from 460 to 900 nm, but due to overlapped modes we could not distinguish individual emission peaks. Thus, the whole spectrum is deconvoluted with Lorentzian fitting and a typical fitting for *p*H 13 sample is shown in Fig. 4.8. Four bands centered at 536.1/2.31,

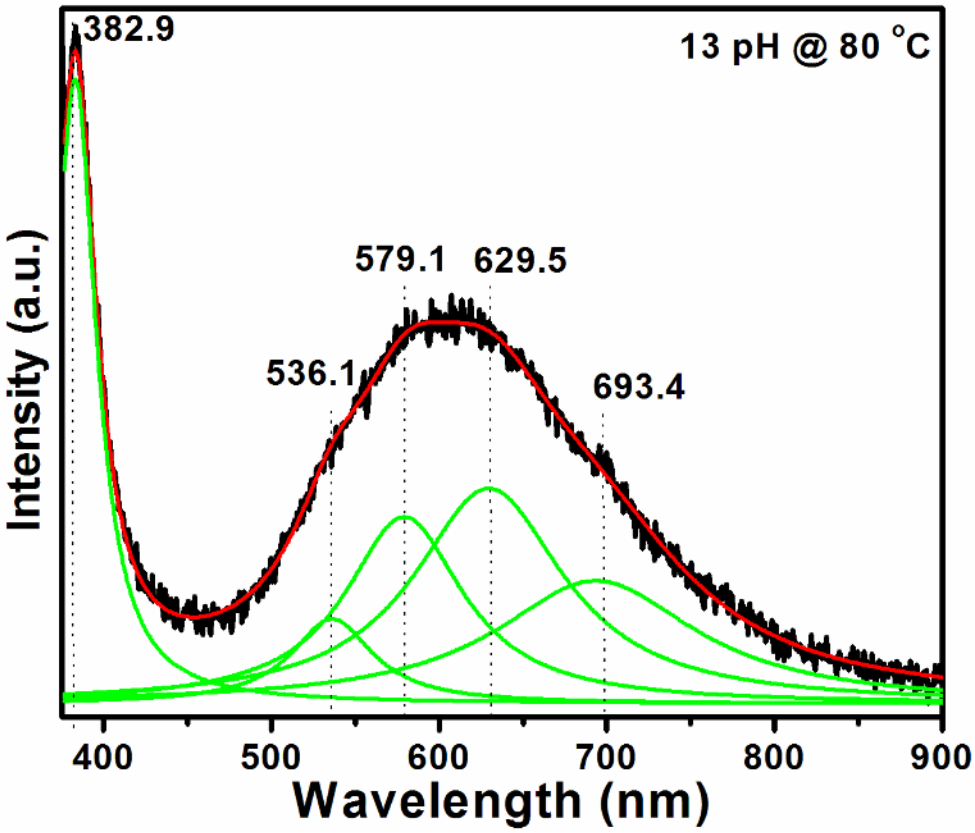

Figure 4.8: The deconvoluted PL spectra of sample synthesised at *p*H 13 and dried at 80 °C for 24 h**.**

579.1/2.14, 629.5/1.97 and 693.4/1.79 nm/eV are observed and assigned as band I, II, III and IV. The origin of DBE accompanied with the band I, II and III is strongly related to defects like Zn vacancies, O vacancies and O interstitials, respectively [Ahn *et al*. (2009); Ke *et al*. (2010)]. However, the appearance of band IV is not very common. The similar visible emission (regarding the band IV) has been commonly observed in hydrothermally and hydrothermal-electrochemically synthesised ZnO samples. Park *et al*. (2009) and Yao *et al*. (2010) have attributed the yellow emission in the broad band due to the presence of OH groups, prepared by hydrothermal-electrochemical synthesis at different temperatures. The band IV in higher pH samples dried at 80 ^{o}C is thus assigned to OH group corroborated with the XRD and Raman results. Thermal desorption spectroscopy, reported by Xie *et al*. (2006), reveals the desorption temperature of the OH groups to be 150 ^{o}C. The suppression of DBE in the samples dried at 250 ^{o}C might be due to the absence of hydroxyl (OH) which is expected and also supported with Raman as well as XRD studies. The emission band accompanied with several peaks appearing in the range of 510-575 nm and 764-875 nm is observed for *p*H 5.5 sample dried at 80 ^{o}C, which is quite different from ZnO emission. This is because the sample is not of ZnO rather $Zn_5(OH)_8(NO_3)_2(H_2O)_2$ as observed from XRD and Raman. However, after drying at 250 ^{o}C, the intense NBE emission of ZnO is observed.

4.1.4 Detection of Cationic Defects by PAS

Positron annihilation spectroscopy is further carried out as it is a unique tool to study the defects. The defects in ZnO could be Zn vacancy (V_{Zn}), O vacancy (V_O), defect clusters, voids etc. The life time of positrons trapped in defects is comparatively larger than the life time of positrons that annihilated at defect free regions. Fig. 4.9 (a-b) depicts the positron annihilation lifetime spectra (PAL) of ZnO powder synthesised at different *p*H and dried at 80 ^{o}C and 250 ^{o}C, respectively. The spectra shown in Fig. 4.9 (a-b) are best fitted with three lifetime components such as τ_1, τ_2, and τ_3. The fitted parameters are shown in Table 4.1. The shortest lifetime component, τ_1 with the intensity I_1

corresponds to positron annihilation at structural defects in the grain boundaries. It may be noted that in a bulk material, τ_1 represents free annihilation of positrons in the defect-free region. But in nanomaterials with size ~50 nm, positrons diffuse through the grains and get trapped at the grain boundaries that are strong trapping centres for the positrons [Mishra *et al.* 2007]. The intermediate lifetime, τ_2 with intensity I_2, represents positron annihilation at nanovoids at the intersection of three or more grain boundaries (e.g. triple junctions). The longest lifetime component, τ_3 with intensity about

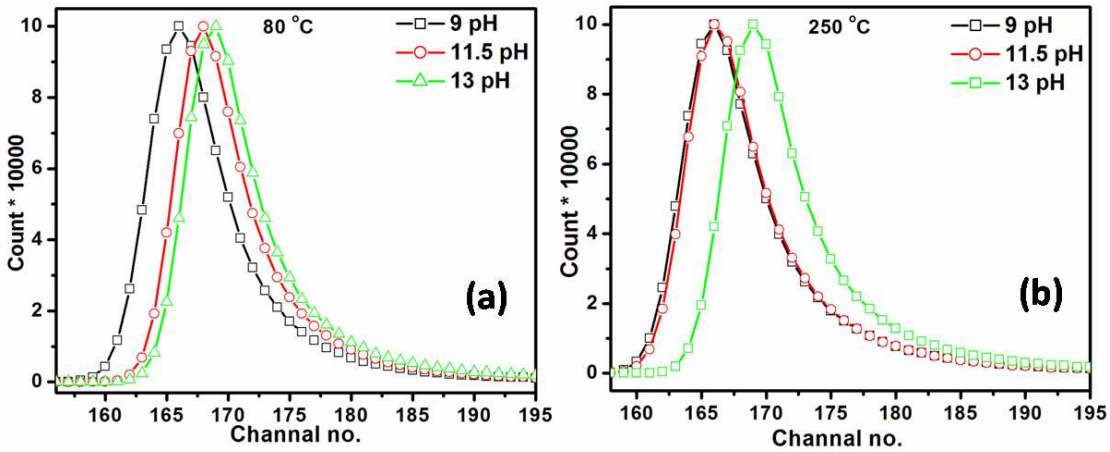

Figure 4.9: Positron lifetime spectrum of ZnO powder synthesized at different *p*H of 9.0, 11.5 and 13.0 **(a)** dried at 80 °C for 24 h, **(b)** dried at 250 °C for 5 h.

Table 4.1: Positron annihilation lifetimes (τ) and corresponding intensities (I) of ZnO powder synthesized through coprecipitation route at different *p*H, dried at 80 °C @ 24 h and 250 °C @ 5 h, respectively.

ZnO At different pH		Positron Lifetime (ps)			Defect Relative Intensities		
		τ_1	τ_2	τ_3	I_1	I_2	I_3
9	Raw	166.1±11.1	317.6±23.7	812.7±226.2	50.4±8.5	48.03±7.4	1.57±1.4
	250	183.7±4.1	400±7.6	3168.2±249.1	39.11±2.1	40.36±2.1	.54±.1
11.5	Raw	168.0±5.6	340.0±11.6	1360.5±248.3	55.74±3.9	43.57±3.7	.69±.3
	250	197.5±3.2	424±9.4	4238.8±155.2	67.46±1.9	31.36±1.9	1.18±.1
13	Raw	198.3±2.3	507.9±15.7	2161.2±97.6	76.05±1.2	22.01±1.4	1.94±.2
	250	185.6±3.9	393.3±7.4	3936.6±131.7	58.10±2.2	40.58±2.2	1.31±.1

τ_1, τ_2, and τ_3 are Positron Life Time with Relative Intensities I_1, I_2, and I_3

2% has been attributed to the pick-off annihilation of orthopositronium formed in the intercrystalline region characterised by large volumes (Look *et al*., 1998). In ZnO, oxygen vacancy (V_O) is invisible in PAS measurement as the positron binding energy of V_O (0.04 eV) is much less than that of V_{Zn} (0.39 eV). Thus, one may observe only positron annihilation due to Zn vacancies which is a common phenomenon in metal oxides. The τ_1, in the present case is found to be about 166, 168 and 198 ps for samples synthesised at *p*H 9, 11.5 and 13 and dried at 80 ^oC, respectively, which are higher than the positron life time in bulk (158 ps) [Tuomisto *et al*. (2003)] and are found to increase gradually with increasing *p*H. In comparison with τ_1, the value of τ_2 (317, 340 and 507 ps, respectively) also increases with *p*H and becomes higher in comparison to the normal cases. As the impurity of $Zn(OH)_2$ is found to present in 80 ^oC dried samples, these positron annihilation life times cannot be due to the presence of defects alone. The higher annihilation lifetime in 80 ^oC dried samples is must be due to the combined effects of native defects as well as formation of $Zn(OH)_2$ phase that increases with increase in *p*H. In 250 ^oC dried samples synthesised at *p*H 9, 11.5 and 13, τ_1 is found to be 183, 197 and 185 ps, respectively. Such higher positron annihilation lifetime (180-200 ps) for pure ZnO in comparison with bulk (158 ps) is surprising. In general, with heat treatment positron annihilation lifetime τ_1 is found to decrease but in the present case for *p*H 9 and 11.5 samples, the annihilation lifetime τ_1 has increased. The annihilation life time τ_1 for 250 ^oC dried samples lie in between the annihilation lifetime reported for bulk and zinc vacancy (V_{Zn}). It has been calculated theoretically that if hydrogen is attached to V_{Zn}, the positron life time decreases successively. For example, while one hydrogen attached to V_{Zn} yields a positron life time of ~200 ps, two hydrogen attached to V_{Zn} reduces the life time to 176-182 ps [Brauer *et al*. (2009); Anwand *et al*. (2010)]. Thus, τ_1 in our case matches well with the life time of V_{Zn} attached to a hydrogen. In the present case, the source of this hydrogen could be water (H_2O) or hydroxyl (OH) ion. During precipitation, the hydrogen atoms are attached to zinc

vacancy sites (V_{Zn}) and form the hydrogen complexes such as V_{Zn}-H. In the form of hydrogen defect complexes such as V_{Zn}-H, hydrogen is more tightly bonded than the hydroxyl groups and is retained upto the temperature 800 °C in ZnO. Desorption of hydrogen starts above the heat treatment at approximately 420 °C [Xie *et al*. (2006)]. In addition to the demolition of hydroxyl group for 250 ^{o}C dried samples, formation of hydrogen related defect complexes like V_{Zn}-H are found responsible for the passivation of native defects, resulting into the suppression of defect band emission (DBE) observed in PL. The intermediate lifetime (τ_2) for *p*H 9, 11.5 and 13 samples dried at 250 ^{o}C are found to be 400, 424 and 393 ps, respectively. This positron annihilation lifetime (τ_2) could be due to multiples of Zn+O divacancies. Theoretical calculation by rigid lattice model shows that depending upon the size, vacancies could be a cluster of 2 to 6 di-vacancies (V_{Zn+O}) with decrease in life time from 375 to 265 ps respectively [Chen *et al*. (2004)]. The life time 365 ps obtained for τ_2 is well within the range of life time of positron corresponding to the cluster of Zn and O di-vacancies.

4.2 Sol–gel

The synthesised ZnO powder through sol-gel method is further calcined at five different temperatures, i.e. at 250 ^{o}C, 600 ^{o}C, 800 ^{o}C and 1000 ^{o}C for 5 h and characterised by various techniques.

4.2.1 Microstructural Studies by XRD and SEM

XRD patterns of ZnO powder synthesised through sol-gel technique are shown in Fig. 4.10. All XRD peaks in samples dried at 250 ^{o}C, 600 ^{o}C, 800 ^{o}C and 1000 ^{o}C, correspond the wurtzite phase of ZnO (JCPDS 89-1397). No additional peaks are observed indicating that no structural changes and/or formation of additional phases in ZnO within the detection limit of XRD. As the particles are of nanosize, in order to separate out the contribution of size and strain, we have calculated the FWHM of each peak and plotted them as per Williamson-Hall (W-H) equation. The Williamson-Hall (W-H) plot of the

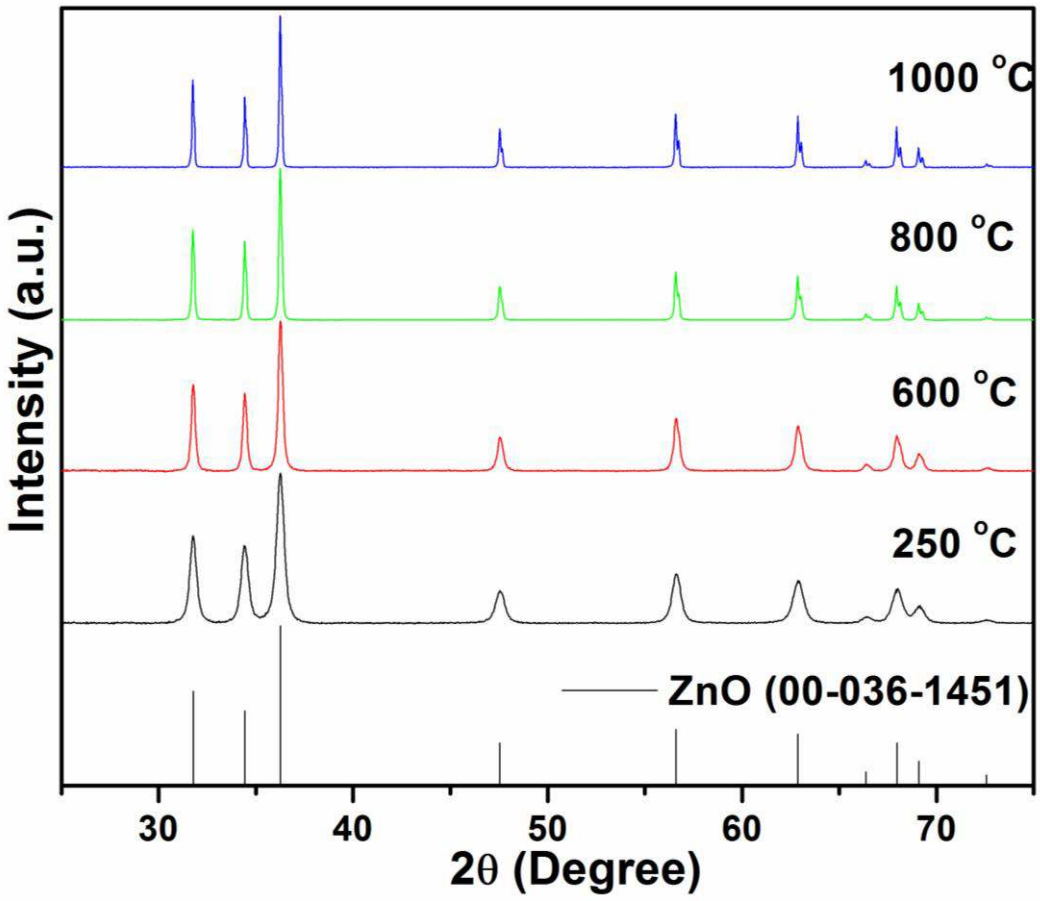

Figure 4.10: The XRD patterns of ZnO powder synthesised through sol-gel route and calcined at different temperatures (250, 600, 800, 1000 °C) for 5 h**.**

samples calcined at 250 °C, 600 °C, 800 °C and 1000 °C are shown in Fig. 4.11. The W-H plot is constructed by choosing $2\sin\theta/\lambda$ as x-axis and $\beta\cos\theta/\lambda$ as y-axis where β is the full width at half maximum (FWHM) of various Bragg peaks measured after removing the $K\alpha_2$ contribution and the instrumental broadening effects, θ is the Bragg angle and λ is the X-ray wavelength [Williamson *et al*. (1953)]. For pure particle size broadening, the plot is expected to be a horizontal line parallel to the X-axis whereas, in the presence of strain, it has a non zero slope. Negative as well as positive slopes have been observed for different materials [Gu *et al*. (2004); Ghosh *et al*. (2007); Kar *et al*. (2010)]. It is explained that the negative slopes is related to compressive strain in nature and the positive slopes is related to tensile strain in nature. Moreover, the strain could be due to the defects originating from some lattice disorder [Barick *et al*. (2010); Etacheri *et al*. (2012); Sendi *et al*. (2013)]. The

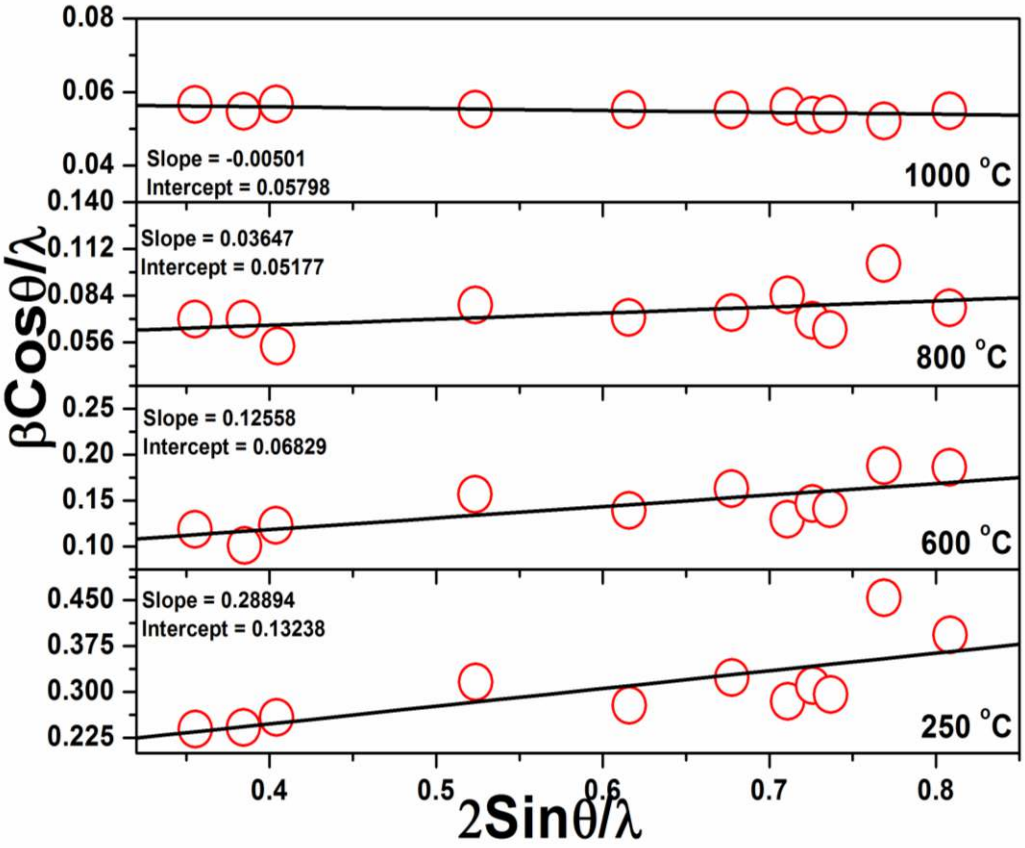

Figure 4.11: W-H plot corresponding to XRD patterns of ZnO powder synthesised through sol-gel route and calcined at different temperatures (250, 600, 800, 1000 ^{o}C) for 5 h**.**

slope as evidenced from the plots in the present case indicates the strain in the lattice. The nature of slopes is found to be positive that decreases with increasing calcination temperature. The decreasing slopes reveal reduction in strain present in ZnO lattice. For the sample calcined at 1000 ^{o}C, the W-H plot is found almost parallel to x-axis indicating zero strain in the lattice. The effect of strain and its origin have been further explained after carrying out Raman, photoluminescence and positron annihilation spectroscopy.

Fig. 4.12 (a-b) show the typical SEM images of ZnO calcined at 1000 ^{o}C. The image demonstrates the particles are of micron size. The higher resolution image shown in Fig. 4.12 (b), indicates more dense ZnO particles with broad distribution of particle size. Histogram of particle size distribution, shown in inset of Fig. 4.12, reveals that the maximum numbers of particles with spherical shape are found in the range of 350-500 nm.

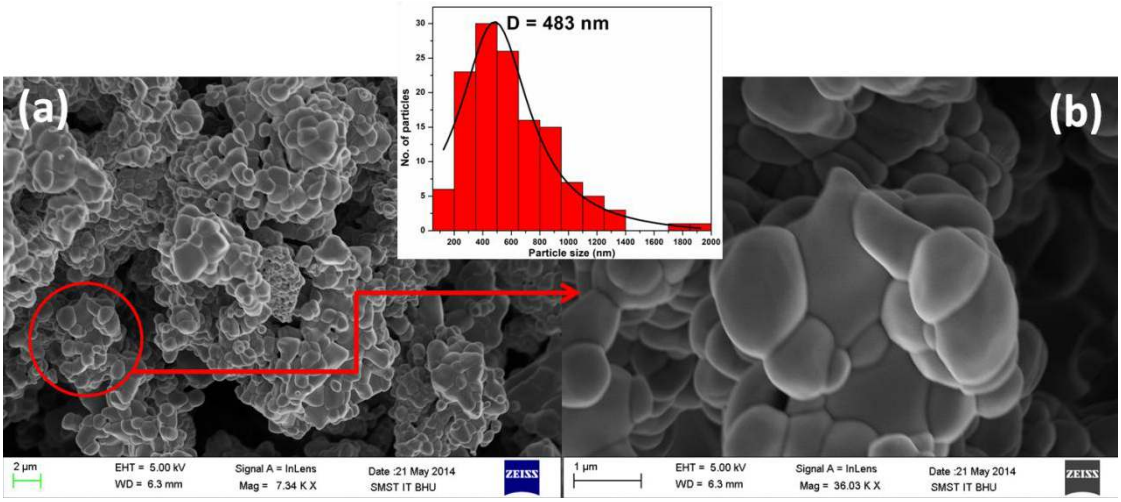

Figure 4.12: The SEM image of the ZnO powder synthesised through sol-gel route and calcined at 1000 ^{o}C with **(a)** low resolution, **(b)** high resolution and the inset image shows the histogram of particle size distribution for the sample calcined at 1000 ^{o}C.

4.2.2 Detection of Vibrational Modes Using Raman spectroscopy

Raman measurement at RT for the samples calcined at 250 ^{o}C, 600 ^{o}C, 800 ^{o}C and 1000 ^{o}C are shown in Fig. 4.13. From the Raman spectra, it is apparent that even after calcining at 600 ^{o}C the derivatives of organometallic zinc precursor containing acetic acid [Eric A. Meulenkamp, (1998)] remain in the sample which shows broad back ground and cannot be detected through XRD. Only E_2(high) (436.7 cm^{-1}) is observed in 250 ^{o}C calcined powder. In 600 ^{o}C calcined sample, due to organometallic zinc precursor, the broad back ground above 800 cm^{-1} is observed. To assign the Raman modes accurately for 600 ^{o}C, 800 ^{o}C and 1000 ^{o}C calcined samples, we have deconvoluted the peaks. Typical fitting in the range 200-800 cm^{-1} as well as 800-1300 cm^{-1} are done for 1000 ^{o}C calcined sample and is shown in Fig. 4.14. The observed Raman modes are matched well with the reported vibrational modes [Manjón *et al*. (2005); Samanta *et al*. (2006); Xu *et al*. (2010); Duan *et al*. (2010)]. The first order Raman modes such as A_1(TO), E_1(TO), E_2(high), E_1(LO) and multi phonon modes present in the experimentally observed spectra are compared with reported results from the literature (Table 4.2). In addition, the relative intensity of E_1(LO) mode at 582 cm^{-1} for 600 ^{o}C calcined sample is found

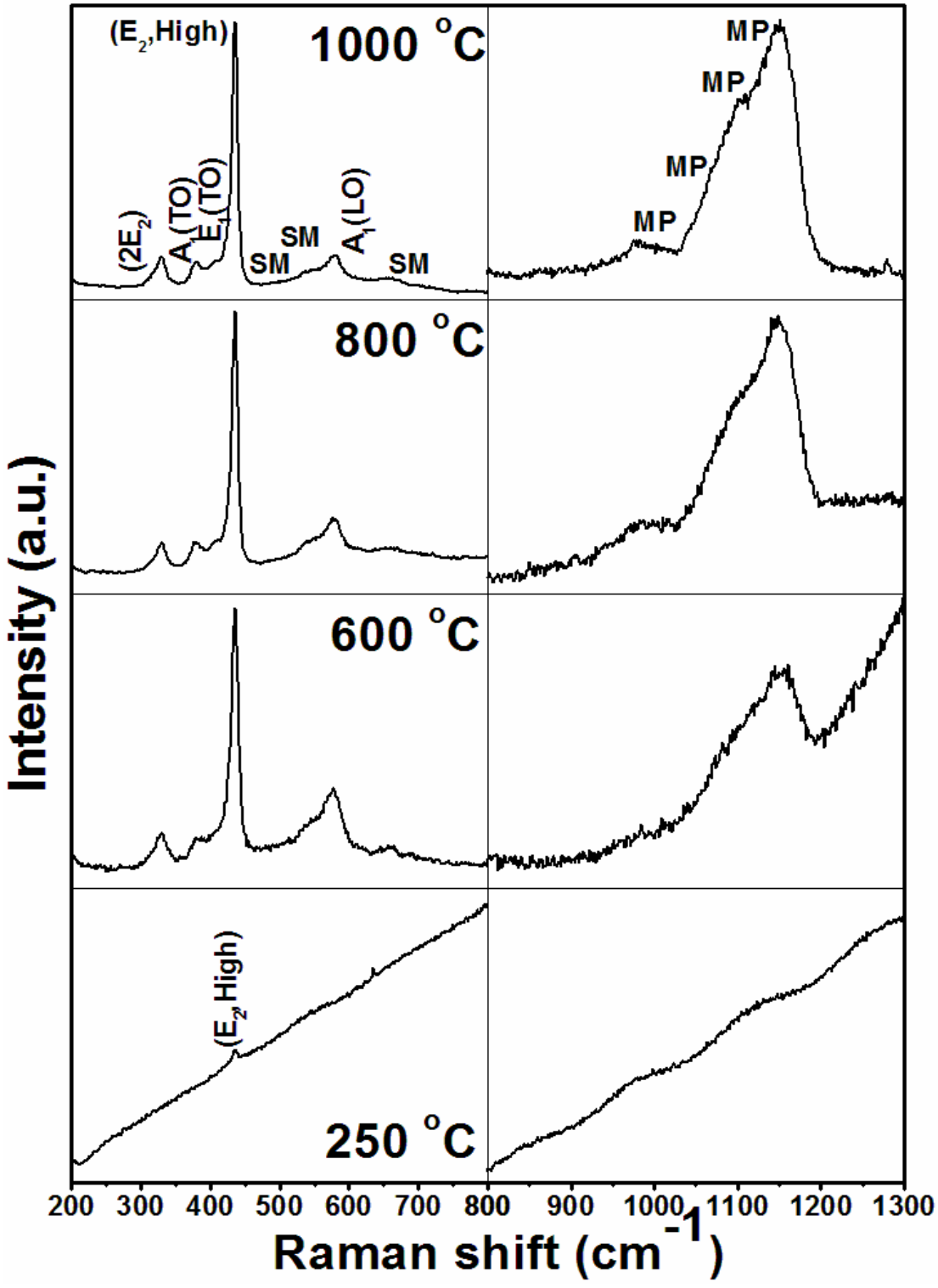

Figure 4.13: The Raman spectrum of ZnO powder synthesised through sol-gel route and calcined at different temperatures (250, 600, 800, 1000 ^{o}C) for 5 h**.**

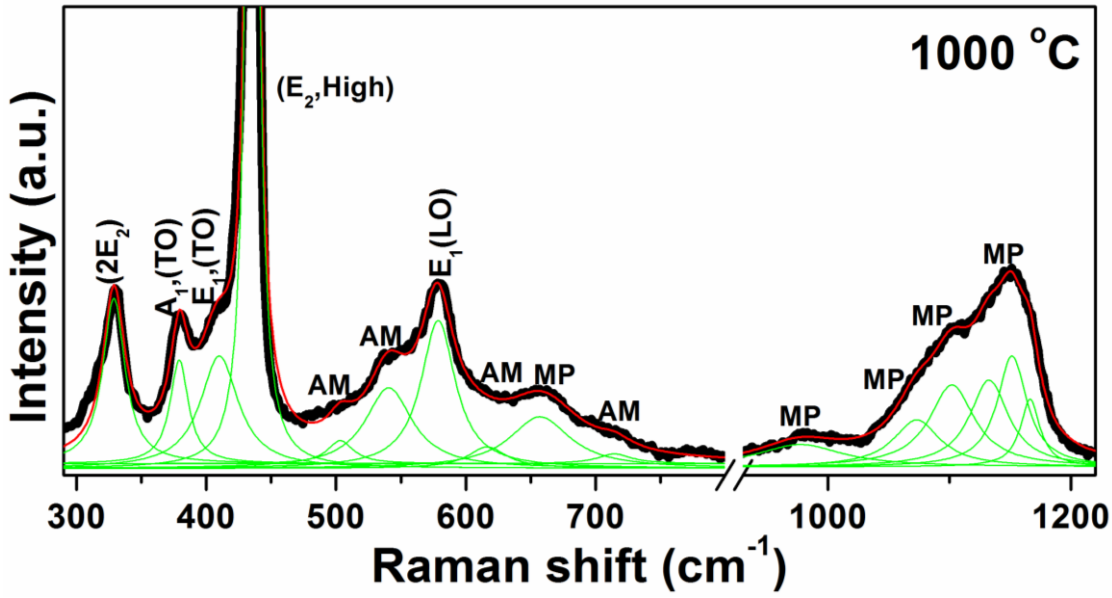

Figure 4.14: The deconvoluted Raman spectrum of the sample synthesised through sol-gel route and calcined at 1000 °C for 5 h**.**

anomalously high and show the gradual decrease in the intensity with increasing calcination temperature. However, the decrease in the intensity of E_1(LO) mode compared to the E_2(high) mode is insignificant. The origin of E_1(LO) mode is ascribed to the presence of defects such as interstitial zinc or oxygen vacancy in the lattice [Wang *et al.* (2010)]. Similar observation is reported by Sharma *et al.* (1997). Lack in source of oxidant during the precipitation of sol might be responsible for Zn_i in sol-gel synthesised ZnO. With increasing calcination temperature in air, the excess zinc in the sample is oxidised and the E_1(LO) Raman mode get reduced [Sharma *et al*. (1997)]. Besides the regular Raman modes, a few additional modes (AM) at 504, 540, 613 and 657 cm^{-1} have been observed in samples calcined at 600 °C, 800 °C and 1000 °C. The additional Raman modes observed by us are in agreement with the silent modes (SM) reported in literature and are compiled in Table 4.2. Although the additional modes in doped ZnO are well reported in literature, their presence in pure ZnO is surprising.

Table 4.2: Reported and observed vibrational modes obtained from deconvoluted Raman spectrum of ZnO powder synthesised through sol-gel and combustion route, calcined at different temperatures.

Raman vibrational modes of ZnO	Reported (cm^{-1})	Sol-gel method (Observed)	Combustion method (Observed)	
		1000 °C (cm^{-1})	600 °C (cm^{-1})	1200 °C (cm^{-1})
1st order Raman active phonon modes				
A_1(TO)	382[*†]	381	375	378
E_1(TO)	414[*†]	413	407	410
E_2^{high}	439[*†]	436	437	436
A_1(LO)	574[*†]	-----	-----	-----
E_1(LO)	580[*†]	578	582	586
Additional modes (AM)				
$2B_2$(low)	520[#]	504	509	514
B_1(high)	552[#]	540	540	536
TA+B_1(high)	650[#]	613	617	623
Other	680[‡]	657	699	715
Multiphonon modes (MP)				
$2E_2$	333[†]	329	327	329
TA + LO	666[†]	657	658	663
2TO	980[†]	979	984	982
TO + LO	1072[†]	1079	1074	1075
2LO	1105[†]	1107	1102	1104
$2A_1$(LO), $2E_1$(LO); 2LO	1158[†]	1152	1149	1155

([#]Manjón *et al*., 2005; [*]Xu *et al*., 2010; [†]Samanta *et al*., 2006; [‡]Duan *et al*., 2010)

4.2.3 Optical Properties Using PL Spectroscopy

Photoluminescence spectra obtained at room temperature for ZnO calcined at different temperatures of 250 °C, 600 °C, 800 °C and 1000 °C are shown in Fig. 4.15. In ZnO samples calcined at 250 °C, 600 °C, 800 °C and 1000 °C, we observe a very sharp and intense band in UV region (NBE). There is no defect related band (DBE) observed for these samples. We observe red shift in NBE emission with increase in calcination temperature. This shift could

be due to increase in crystallite size of ZnO. Absence of defects in sol-gel synthesised ZnO samples may be exploited for the optical devices.

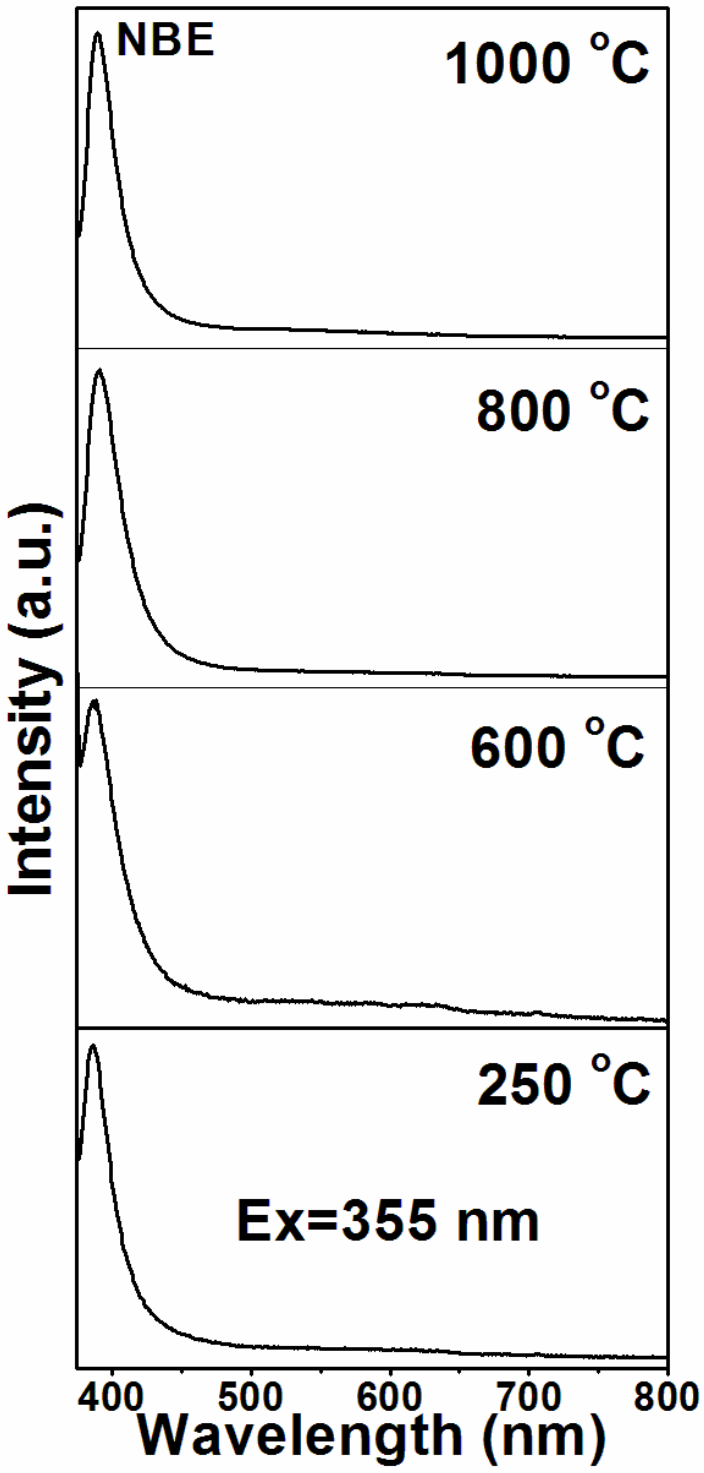

Figure 4.15: The PL spectrum obtained by using the excitation wavelength 355 nm for the ZnO powder synthesised through sol-gel route and, calcined at different temperatures (250, 600, 800, 1000 ^{o}C) for 5 h**.**

4.2.4 Detection of Cationic Defects by PAS

Fig. 4.16 shows the positron annihilation lifetime spectra (PAL) best fitted with three lifetime components such as τ_1, τ_2, and τ_3. The fitted parameters are given in Table 4.3. The τ_1, in the present case is found to be 177.5 and 170.9 ps for 250 and 600 ^{o}C calcined samples, respectively, which is much higher than the positron life time in bulk or defect free ZnO i.e. 158 ps [Tuomisto *et al*. (2003)]. This increased life time must be due to organic residual present in the sample even after calcining at 600 ^{o}C, which is precisely observed through Raman technique. The value of τ_1 decreases to 154.9 and 142.6 ps for samples calcined at 800 and 1000 ^{o}C, respectively. Annihilation life time of 154.9 ps is comparable to sintered ZnO [Dutta *et al*. (2005); Brauer *et al*. (2007)]. However, in samples made at 250 and 600 ^{o}C, τ_2 may be due

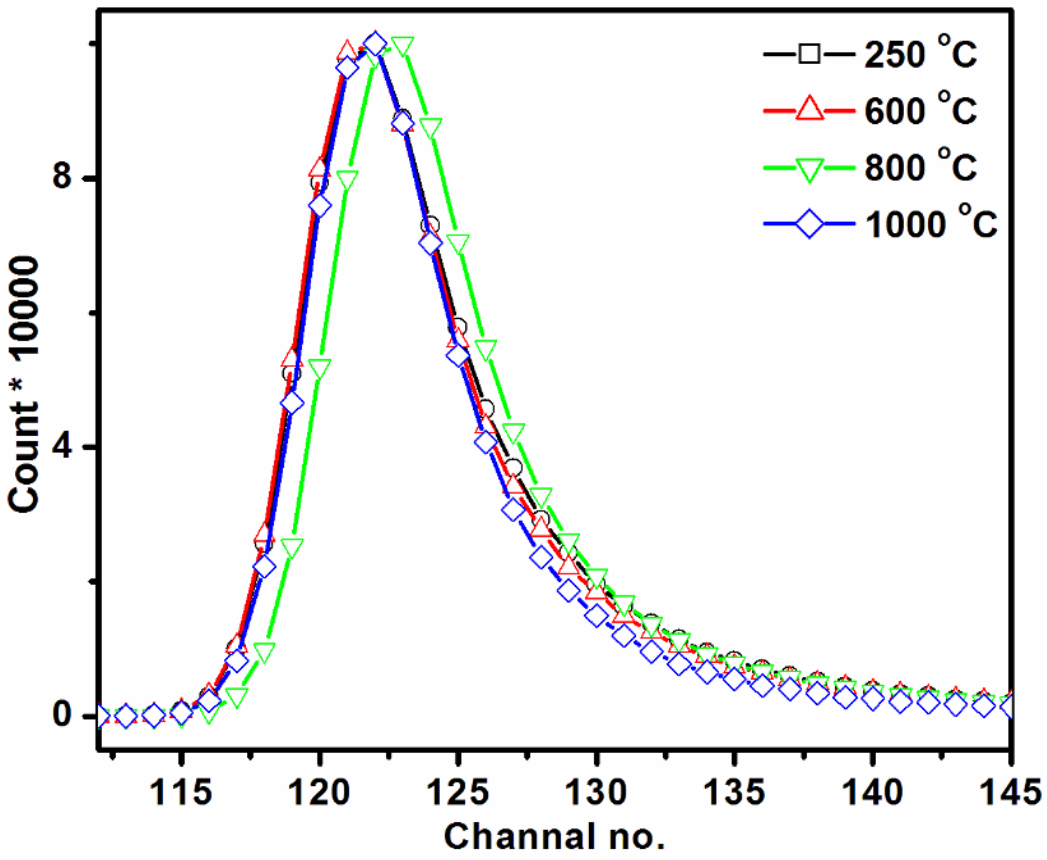

Figure 4.16: Positron annihilation lifetime spectrum of ZnO powder synthesised through sol-gel route and calcined at different temperatures (250, 600, 800, 1000 ^{o}C) for 5 h**.**

Table 4.3: Positron annihilation lifetimes (τ) and corresponding intensities (I) of ZnO powder synthesized through sol-gel route, calcined at different temperature for 5h.

ZnO 13 pH temperature	Positron Lifetime (ps)			Defect Relative Intensities		
	τ_1	τ_2	τ_3	I_1	I_2	I_3
250	177.5±4.7	361.8±7.5	2729.8±296.6	54.60±2.8	44.98±2.7	0.41±.1
600	170.9±2.9	393.8±6.0	5661.8±1779.4	62.8±1.5	37.08±1.5	0.07±.02
800	154..9±7.9	312.7±24.1	754.8±165.9	54.41±6.7	43.22±2.3	2.35±1.7
1000	142.6±13.7	261.8±46.2	534.9±120.5	52.6±5.6	42.05±4.4	5.35±1.0

τ_1, τ_2, and τ_3 are Positron Life Time with Relative Intensities I_1, I_2, and I_3

to the combined effect of cluster of (Zn+O) divacancies and residual organic precursor [Chen *et al*. (2004)]. The annihilation life time (τ_2) further decreases from 312.7 to 261.8 ps by increasing calcination temperature from 800 and 1000 ^{o}C. The annihilation life time τ_2 is closer to the life time of positron corresponding to the cluster of two and one (Zn+O) di-vacancies, respectively. Fig. 4.17 (a-b) shows the plot in between different calcination temperature and τ_1, τ_2 and τ_{av}, where τ_{av} is calculated for the sample synthesised through sol-gel technique with the help of equation (4.2).

$$\tau_{av} = \frac{\tau_1 I_1 + \tau_2 I_2 + \tau_3 I_3}{I_1 + I_2 + I_3} \qquad (4.2)$$

The decrease in τ_1, τ_2 and τ_{av} indicates the decrease in anionic defects with increasing calcination temperature which is corroborated with the W-H Fplot results where the strain is found to decrease with increasing calcination temperature. This strain must be due to the cluster of Zn+O divacancies which decreases with increasing calcination temperature.

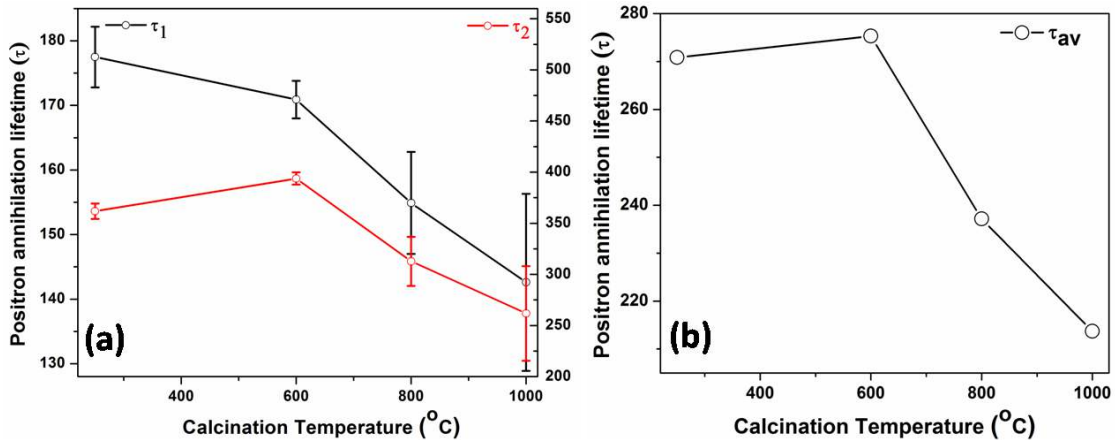

Figure 4.17: The plot in between different calcination temperature and the calculated positron annihilation lifetime **(a)**τ_1 and τ_2 and **(b)** τ_{av}, for the sample synthesised through sol-gel technique.

4.3 Combustion Method

ZnO powder synthesised through combustion method is calcined at 600, 800, 1000 and 1200 °C for 5 h. Further, all the calcined samples are investigated through different characterisation techniques.

4.3.1 Thermal Analysis

To determine the effective processing conditions for the synthesis of ZnO through combustion technique, thermal analysis of gel prepared through mixing $Zn(NO)_3$ precursor and urea is carried out through TG-DTA. We could identify the decomposition, phase formation, and sintering behaviour of ZnO. We have studied the changes in sample from gel to powder form, on heat treatment by carrying out the thermal analyses through TG-DTA. Fig. 4.18 shows TG-DTA curves of gel used for ZnO. It can be seen from the DTA curve that an endothermic reaction takes place at 130 °C accompanied with an exothermic reaction at 145 °C. This clearly indicates that the urea present in gelatinous form absorb heat for activating the combustion process and releases enormous amount of heat. Full urea decomposition is observed upto 400 °C associated with enormous weight loss. The endothermic peak at 467 °C coupled with minute weight loss confirms the decomposition of zinc nitrate and the formation of ZnO powder.

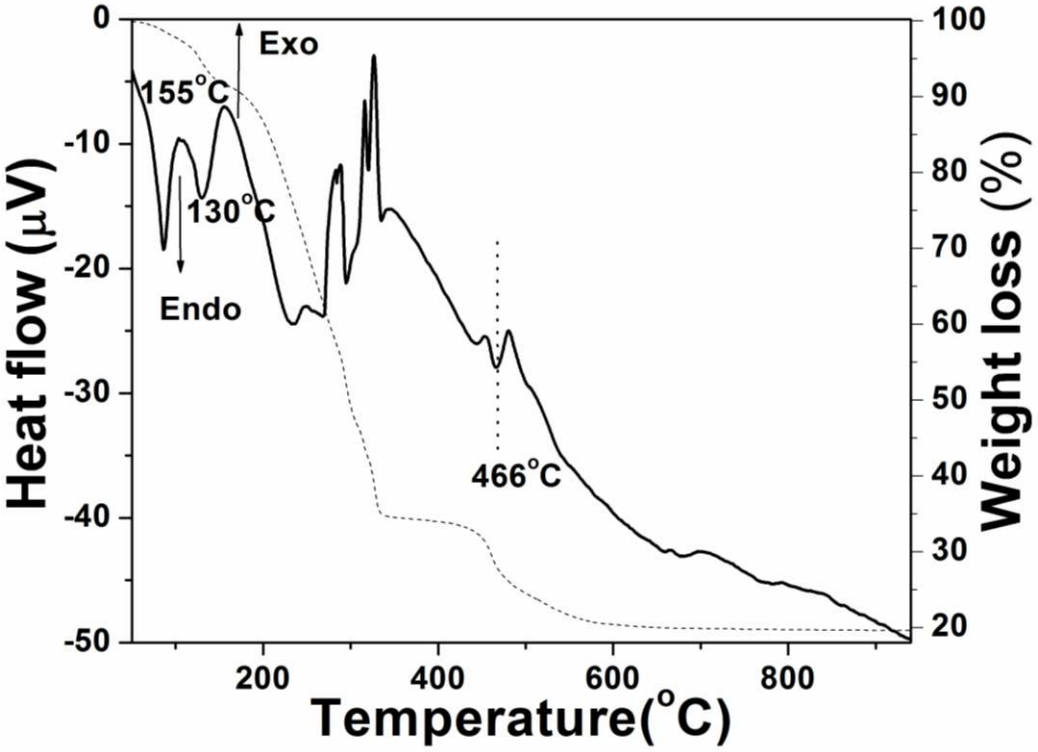

Figure 4.18: The TG-DTA of as prepared gelatinous sample of ZnO @ 10 ^{o}C/min.

4.3.2 Microstructural Studies by XRD and SEM

XRD patterns of ZnO powder synthesised through solution-combustion techniques are shown in Fig. 4.19. All XRD peaks correspond to the wurtzite phase of ZnO (JCPDS 89-1397). No additional peaks are observed indicating no structural changes and/or formation of additional phases in ZnO within the detection limit of XRD. Williamson-Hall (W-H) plot of samples calcined at 600, 800, 1000 and 1200 ^{o}C, are shown in Fig. 4.20 [Williamson *et al*. (1953)]. The slope as evidenced from the plots in the present case indicates the strain in the lattice (Fig. 4.20). Minor reduction in strain is observed with increasing calcination temperature. The slopes are found to be negative for all the samples. Normally in pure and doped ZnO, the slopes obtain from Williamson-Hall (W-H) plots found to be positive [Dutta *et al*. (2009)]. However in present case, the slope is negative which is surprising. Few reports have also shown

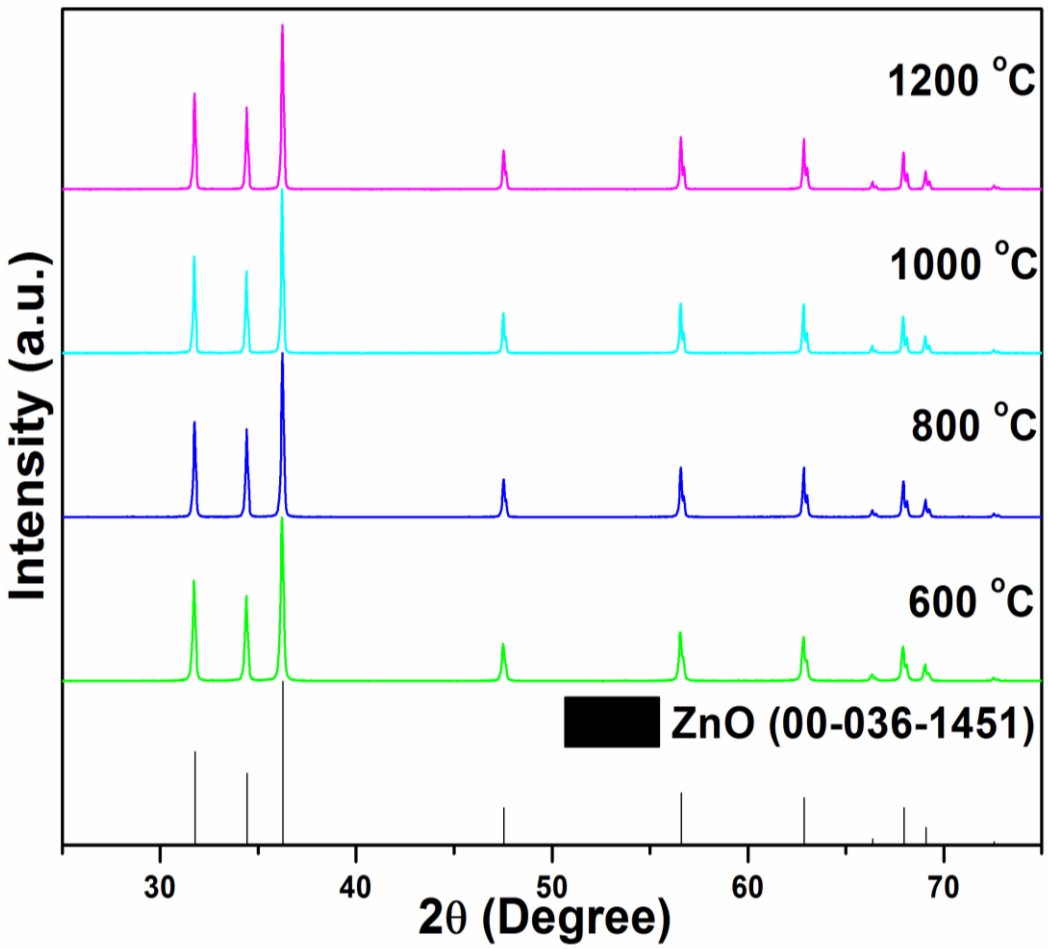

Figure 4.19: The XRD patterns of ZnO powder synthesised through combustion route and calcined at different temperatures (600, 800, 1000, and 1200 °C) for 5 hr**.**

negative slopes and have mentioned that the strain is compressive in nature [Gu *et al*. (2004); Ghosh *et al*. (2007); Kar *et al*. (2010)]. The strain could be due to the defects originating from some lattice disorder [Gao *et al*. (2013), Sendi *et al*. (2013)]. In order to understand the different nature of strain induced in the lattice, we have carried out Raman, Photoluminescence and positron annihilation spectroscopy.

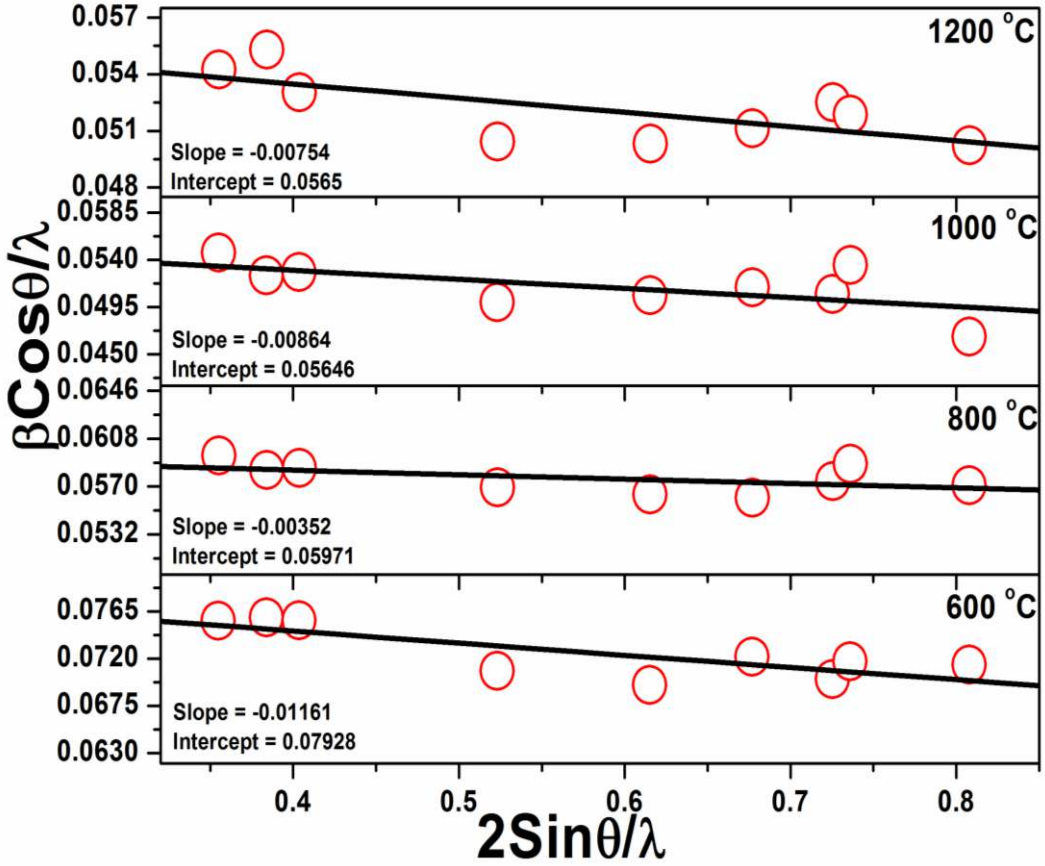

Figure 4.20: W-H plot corresponding to XRD patterns of ZnO powder synthesised through combustion route and calcined at different temperatures (600, 800, 1000 and 1200 ^{o}C) for 5 h**.**

Fig. 4.21 (a-b) shows the SEM images of ZnO calcined at 700 and 1200 ^{o}C. ZnO calcined at 700 ^{o}C shows the presence of large number of pores and fluffy nature of the product which could be due to the release of large amount of N_2 and CO_2 gas during combustion. The image shows two types of morphology which are shown as insets of Fig. 4.21 (a). The upper inset shows more dense ZnO particles with broad distribution of particle of size 40-250 nm. Very fine nanoparticles of size less than 50 nm are residing over the surface of most of the particles. In the lower inset of Fig. 4.21 (a), ZnO particles of 50-200 nm size are arranged in chains. Fig. 4.21 (b) denotes the ZnO sample calcined at 1200 ^{o}C. It is interesting to see the screw dislocation growth of ZnO particles (inset of Fig. 4.21 (b)). Probably the particles of size less than 50 nm

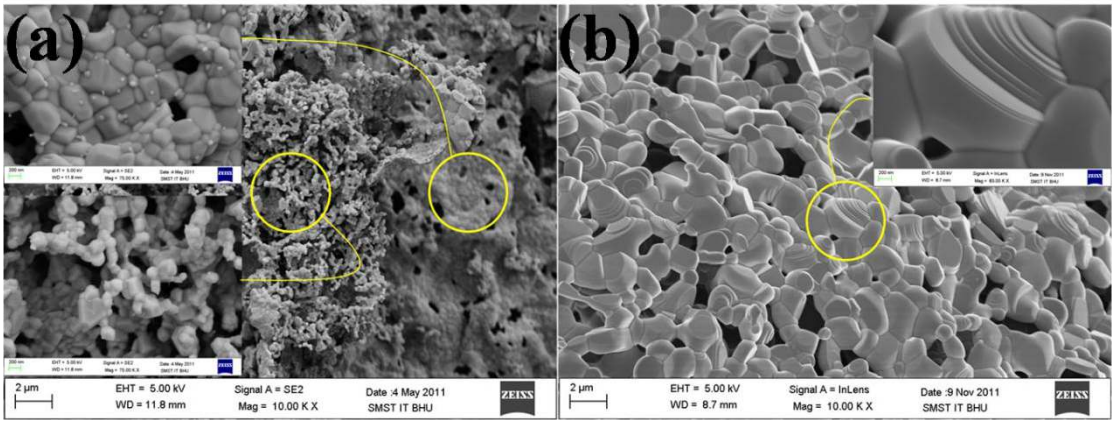

Figure 4.21: The SEM image of the ZnO powder synthesised through combustion route and calcined at **(a)** 600 ^{o}C and **(b)** 1200 ^{o}C. Inset shows the zoomed view of the encircled region.

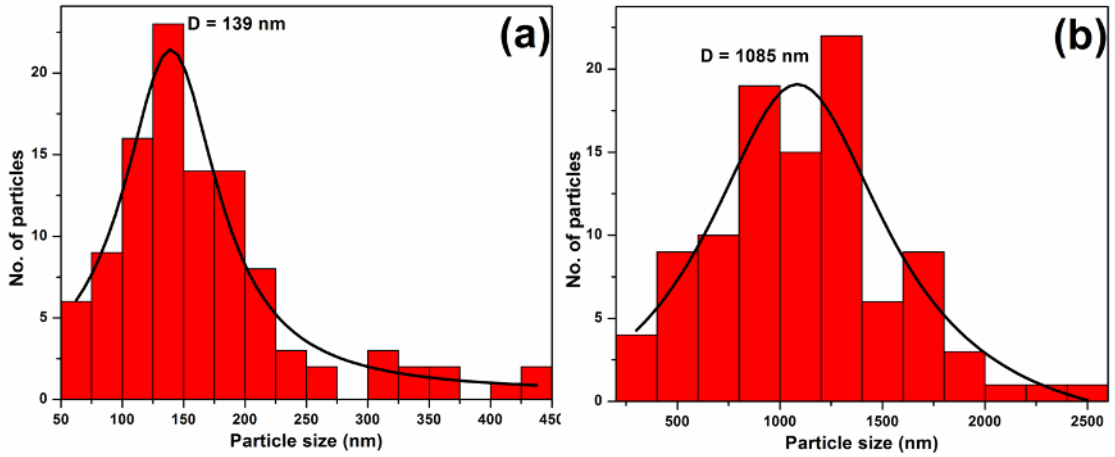

Figure 4.22: The histogram of the particle size distribution obtained from the SEM image of the ZnO powder synthesised through combustion route and calcined at **(a)** 600 ^{o}C and **(b)** 1200 ^{o}C.

residing over surface of the sample calcined at 600 ^{o}C act as nucleation centre for such growth. It is also observed that particles with micron size or more are densely packed. The size of particles in the samples calcined at 600 ^{o}C and 1200 ^{o}C are calculated by plotting the particles size distribution histogram as shown in Fig. 4.22 (a-b).

4.3.3 Detection of Vibrational Modes Using Raman spectroscopy

Raman measurement at RT for the samples calcined at 600, 800, 1000 and 1200 ^{o}C, are shown in Fig. 4.23. To assign the Raman modes accurately we have deconvoluted the peaks with the help of Lorentzian fitting through origin

software. Typical fitting in the range 200-800 cm^{-1} and 800-1300 cm^{-1} are done for 600 and 1200 ^{o}C calcined samples, respectively and are shown in Fig. 4.24. The observed Raman modes are well matched with the reported vibrational modes [Manjón *et al*. (2005); Samanta *et al*. (2006); Xu *et al*. (2010); Duan *et al*. (2010)]. The first order Raman modes such as A_1(TO), E_1(TO), E_2(high), E_1(LO) and multi phonon modes are present in the experimentally observed modes, shown in Table 4.2. In addition, the relative intensity of E_1(LO) mode at 582 cm^{-1} in 600 ^{o}C calcined sample is found anomalously high and show the steady decrease in the intensity with increasing calcination temperature. The significant decrease in the intensity of E_1(LO) mode compared to the E_2(high) mode is observed. The E_1(LO) mode almost disappears in the sample calcined at 1200 ^{o}C. The origin of the mode is ascribed to the presence of

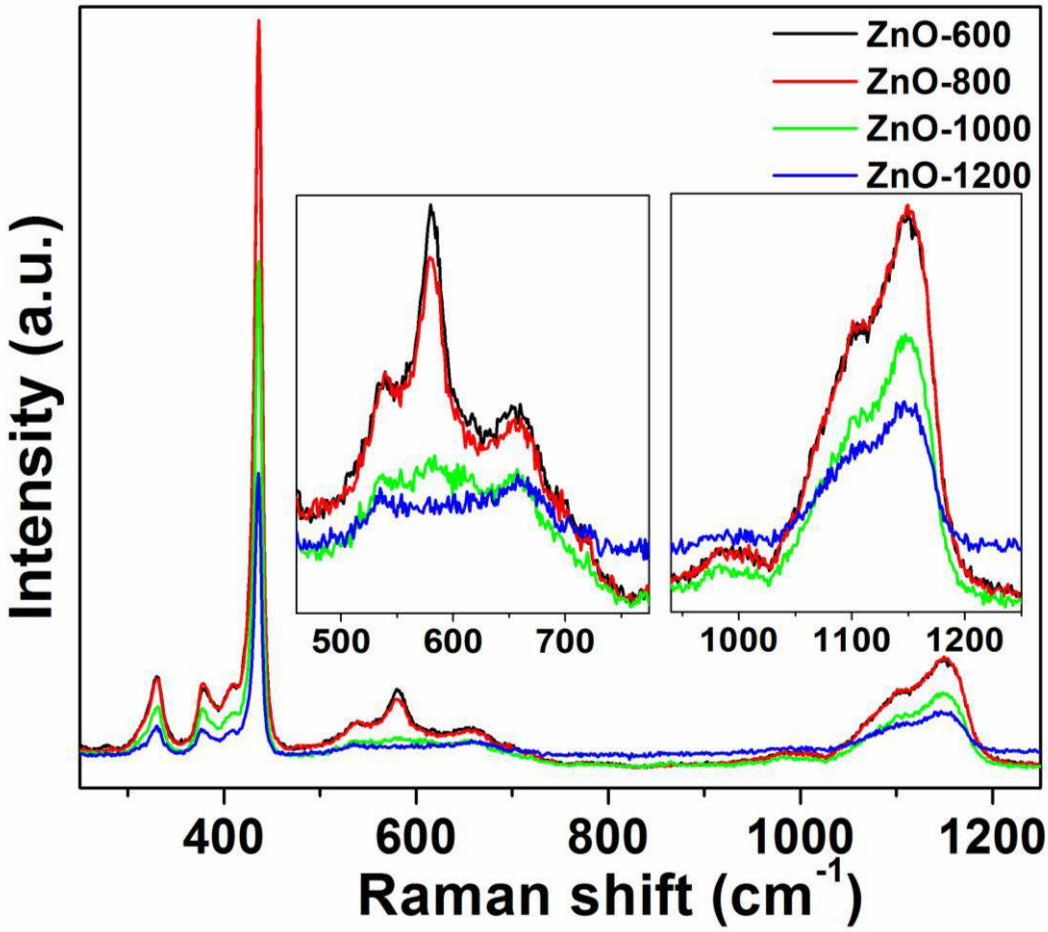

Figure 4.23: The Raman spectrum of ZnO powder synthesised through combustion route and calcined at different temperatures (600, 800, 1000, and 1200 ^{o}C) for 5 h**.**

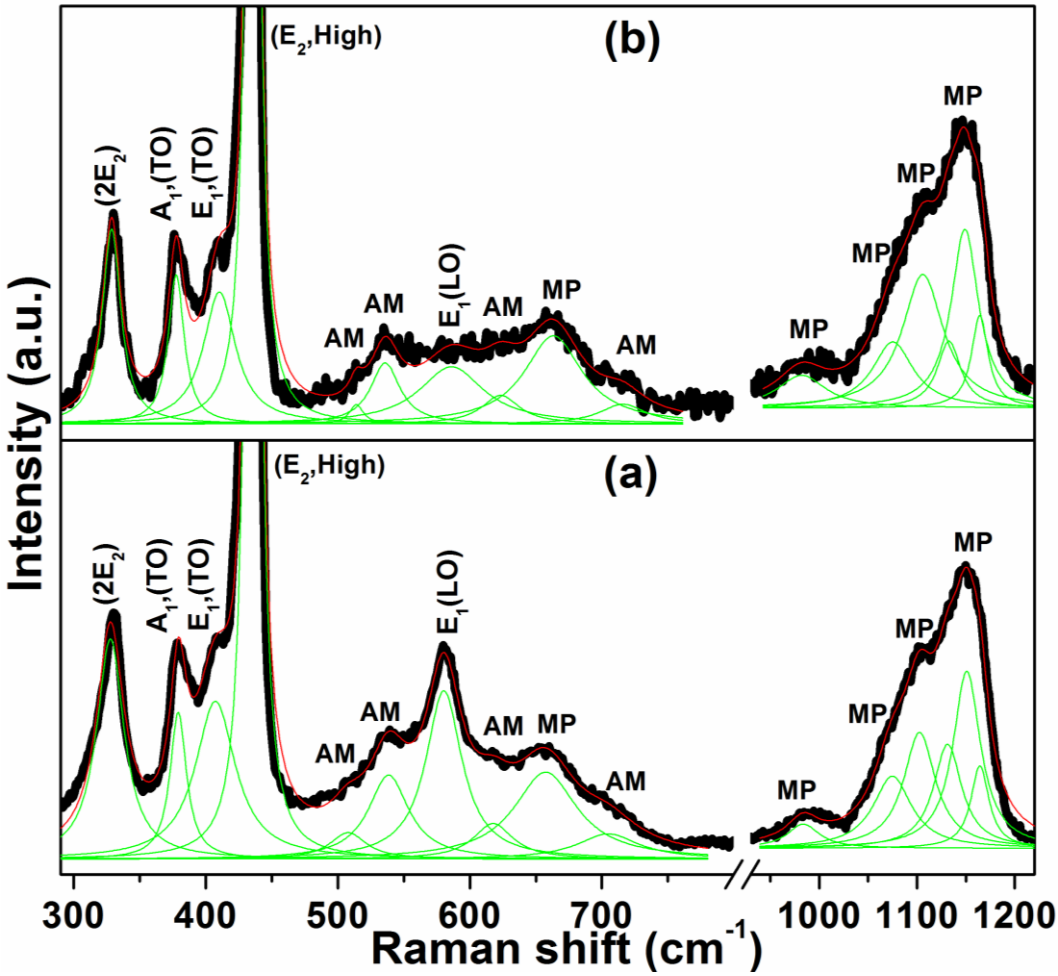

Figure 4.24: The deconvoluted Raman spectra of the samples synthesised through combustion route and calcined at (a) 600 ^{o}C and (b) 1200 ^{o}C) for 5 h**.**

defects such as zinc interstitial or oxygen vacancy in the lattice [Wang *et al*. (2010)]. In both the methods, sol-gel and solution-combustion, we have observed decreasing relative intensity of E_1(LO) mode with increasing calcination temperature. In the combustion route, the excess zinc would arise due to the reduced atmosphere during combustion reaction and with increasing the calcination temperature, the excess zinc in the sample is oxidized leading to the reduced E_1(LO) Raman mode [Sharma *et al.*, (1997)]. Besides the regular Raman modes, a few additional modes (AM) at 509/517, 540/536, 617/623 and 699/715 cm^{-1} have been observed in the samples calcined at 600/1200 ^{o}C, respectively. According to Manjon *et al*. (2005) these additional Raman modes are the silent modes (SM) of ZnO. Raman modes of the sample synthesised through combustion as well as sol-gel are compared after deconvolution as

given in Table 4.2. Although the additional modes in doped ZnO are well reported in literature, their presence in pure ZnO is unexpected and needs further investigation.

4.3.4 Optical Properties Using PL Spectroscopy

Photoluminescence spectra obtained at room temperature for ZnO calcined at 600, 800, 1000 and 1200 °C, are shown in Fig. 4.25. It is clear from the figure that on excitation with 355 nm, two bands appear in the spectrum: one band is due to near band edge (NBE) emission in UV region at 392.6 nm and the other band in green region is due to defect related deep band emission (DBE). The DBE peaks in the sample synthesised through combustion method

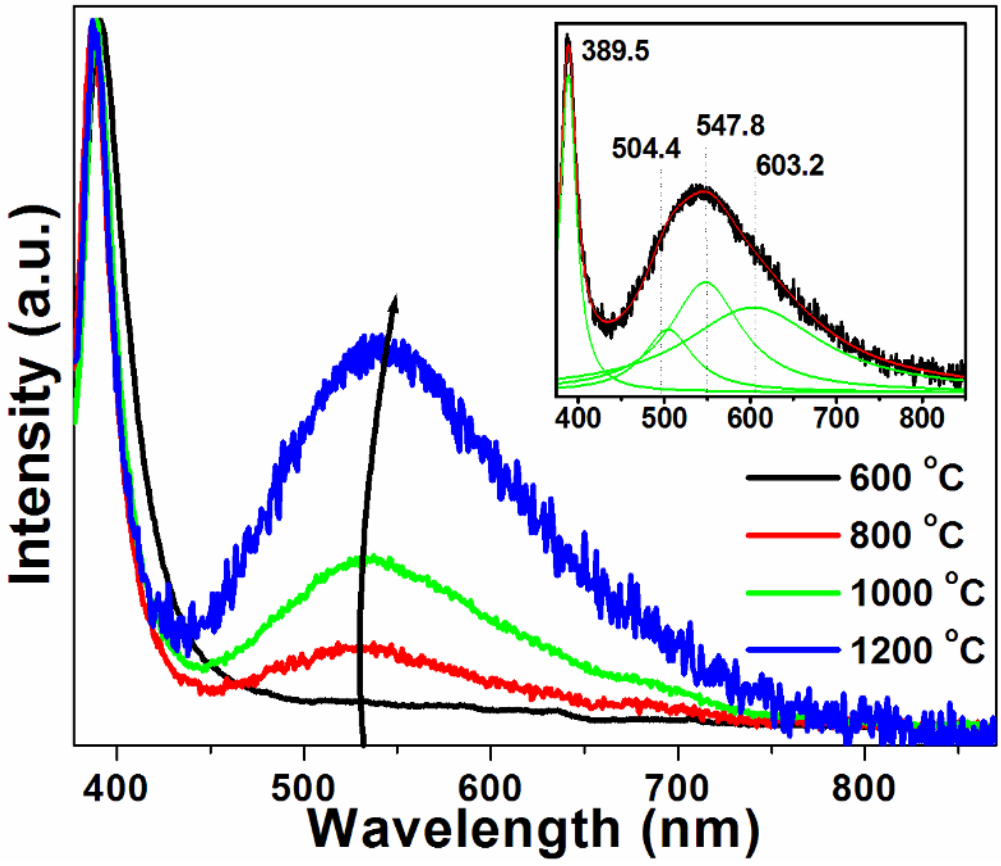

Figure 4.25: The PL spectrum obtained by using the excitation wavelength 355 nm for the ZnO powder synthesised through combustion route and calcined at different temperatures (600, 800, 1000, and 1200 °C) for 5 h. Inset shows the deconvoluted PL spectra of the sample calcined at 1200 °C.

are found to be very intensed compared to the other synthesis methods. Since the samples are in the powder form, we have normalised with respect to NBE peak instead of the peak related to DBE. By comparing the intensity of the broad band (DBE) for all the samples, we can see the increase in DBE. The intensity ratio of I_{DBE}/I_{NBE} is found to be increased as 0.04, 0.12, 0.25 and 0.56, respectively. The PL spectrum of ZnO sample calcined at 1200 ^{o}C is further deconvoluted and shown in inset of Fig. 4.25, where the broad DBE peak is deconvoluted into three sub bands which are centered at 504/2.46, 548/2.26 and 603/2.1 nm/eV. We observed a red shift in the centre of DBE with increasing the calcination temperature which is clearly noticeable from the Fig. 4.25. The shifting and increase in intensity of DBE is due to the increase in the intensity of 3rd band (603/2.1 nm/eV) with calcination temperature. Mostly, the band at 603/2.1 is reported for oxygen interstitial (O_i) [Alvi *et al*. (2013); Ahn *et al*. (2009)]. The higher concentration of O_i defect could be due to calcination at higher temperature in air i.e. O-rich environment [Janotti *et al*. (2009)]. Similar increase and shifting of DBE band in ZnO annealed at 550 ^{o}C and above has been observed by Sendi *et al*. (2013). They ascribed this shifting to the stress generated in between grains during annealing. Increase in the annealing temperature increases the diffusion rate of oxygen on the surface of ZnO and the rate of reaction between free Zn in the sample and oxygen, which lead to an increase in the oxygen concentration in ZnO and generates the strain. However, in the present case, the difference observed in ZnO as explored by Raman and PL is surprising. Raman study reveals the decrease in native defects with increasing calcination. In contrary to Raman, the PL study discloses the presence of defects in combustion synthesised samples which are increase in with increasing the calcination temperature. This difference might be due to different kind of defects responsible for anomaly in Raman and DBE in our case. Ilyas *et al*. (2011) have observed the excess Zn_i under Zn-rich conditions while with increasing annealing temperature in O-rich environment O_i increases in ZnO, relatively. Therefore, in the present case the defect like Zn_i could be responsible for the anomaly observed in Raman at lower annealing

temperature and defect like O_i is responsible for DBE emission at higher annealing temperature. With increasing the calcination temperature, gradually the concentration of Zn_i decreases and the concentration of O_i increases. The O_i could arise due to the combustion reaction at elevated temperature which provides the activation energy to create O_i inside the ZnO. Further, increasing the calcination temperature, formation of more and more O_i takes place. In addition, according to literatures, the defects like V_{Zn}, V_O and their clusters are found to be responsible for 1st and 2nd band of DBE centered at 504/2.46 and 548/2.26 nm/eV [Ahn *et al*. (2009); Ke *et al*. (2010)]. To know the exact nature of these defects, we have further used Positron annihilation spectroscopy.

4.3.5 Detection of Cationic Defects by PAS

Fig. 4.26 depicts the positron annihilation lifetime spectra (PAL) best fitted with three lifetime components such as τ_1, τ_2, and τ_3 for ZnO samples calcined at 600, 800 and 1000 ^oC, synthesised through combustion route. The fitted parameters are given in Table 4.4. The τ_1 for the samples calcined at 600, 800 and 1000 ^oC are 137.1, 143.4 and 142.5 ps, respectively, which are much lower than the positron life time reported for bulk i.e.158 ps. The decreased life time τ_1 (~145 ps) is observed for sintered ZnO samples [Dutta *et al*. (2005); Brauer *et al*. (2007)]. The intermediate lifetime, τ_2, could be due to Zn+O divacancies [Chen *et al*. (2004)]. The annihilation life time 275.6, 259.7 and 277.5 ps (τ_2) obtained for samples calcined at 600, 800 and 1000 ^oC are closer to the life time of positron corresponding to the cluster of one to two Zn+O di-vacancies.

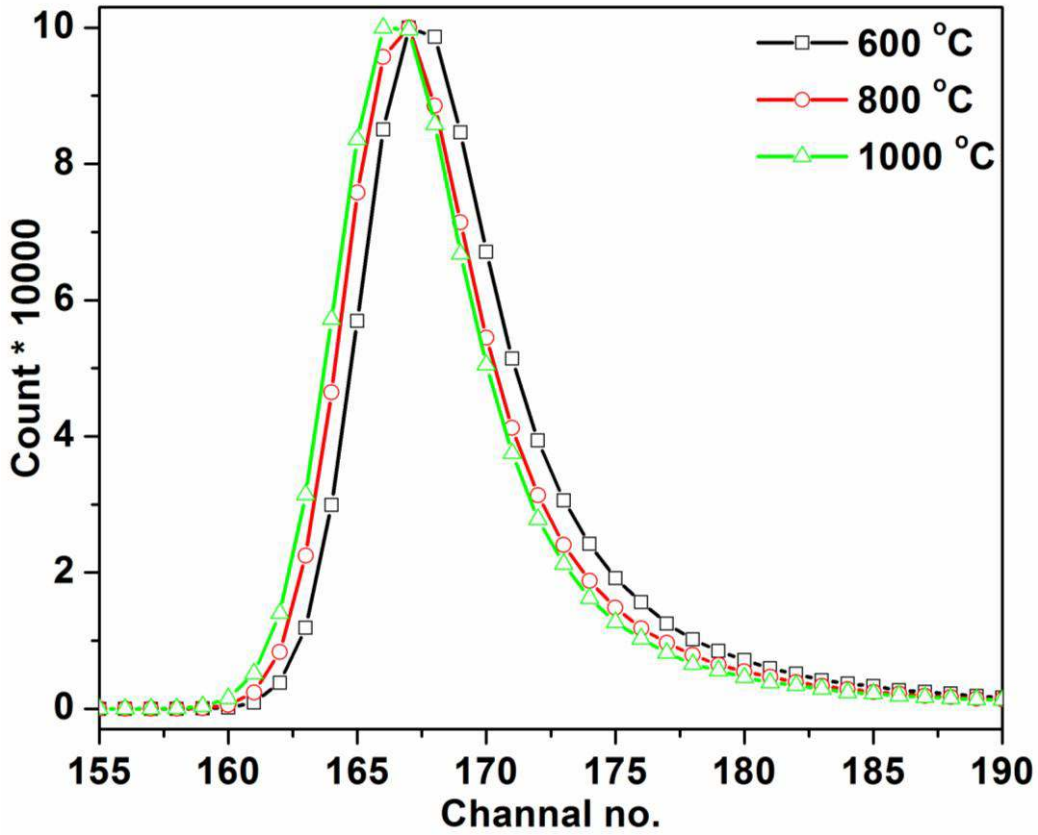

Figure 4.26: Positron annihilation lifetime spectrum of ZnO powder synthesised through combustion route, calcined at different temperatures (600, 800 and 1000 °C) for 5 h.

Table 4.4: Positron annihilation lifetimes (τ) and corresponding intensities (I) of ZnO powder synthesised through combustion route, calcined at 600, 800 and 1000 °C.

ZnO calci. (in °C)	Positron Lifetime (ps)				Defect Relative Intensities	
	τ_1	τ_2	τ_3	I_1	I_2	I_3
600	137.1±9.0	275.6±13.2	840.2±104.8	43.13±6.2	54.53±5.6	2.34±.7
800	143.4±12.6	259.7±32.7	617.7±111.1	52.15±13.8	44.04±11.8	3.82±2.4
1000	142.5±6.8	277.5±26.6	787.9±153.4	65.83±7.5	32.34±6.8	1.83±1.0

τ_1, τ_2, and τ_3 are Positron Life Time with Relative Intensities I_1, I_2, and I_3

Finally based on the above results, we propose a tentative model to illustrate the mechanism of emission processes observed in ZnO, as shown in Fig. 4.27. In the band diagram, we have specified the energy level of V_{Zn}, V_O, Zn_i and O_i corresponding to ZnO. Exciting with photons of energy 3.49 eV (355nm), electrons may show band to band excitation and the formation of excitons. The relative absorption processes of electrons are represented by A_1, A_2 and A_3 in the band diagram. Excited electrons desist and trapped by the defect states of Zn_i, V_o, O_i and V_{Zn} energy levels in the band gap of ZnO. The relative emission processes are E_{1a}, E_{1b}, E_{1c}, E_{2a}, E_{2b} and E_{3a}, E_{3b} as shown in the band diagram.

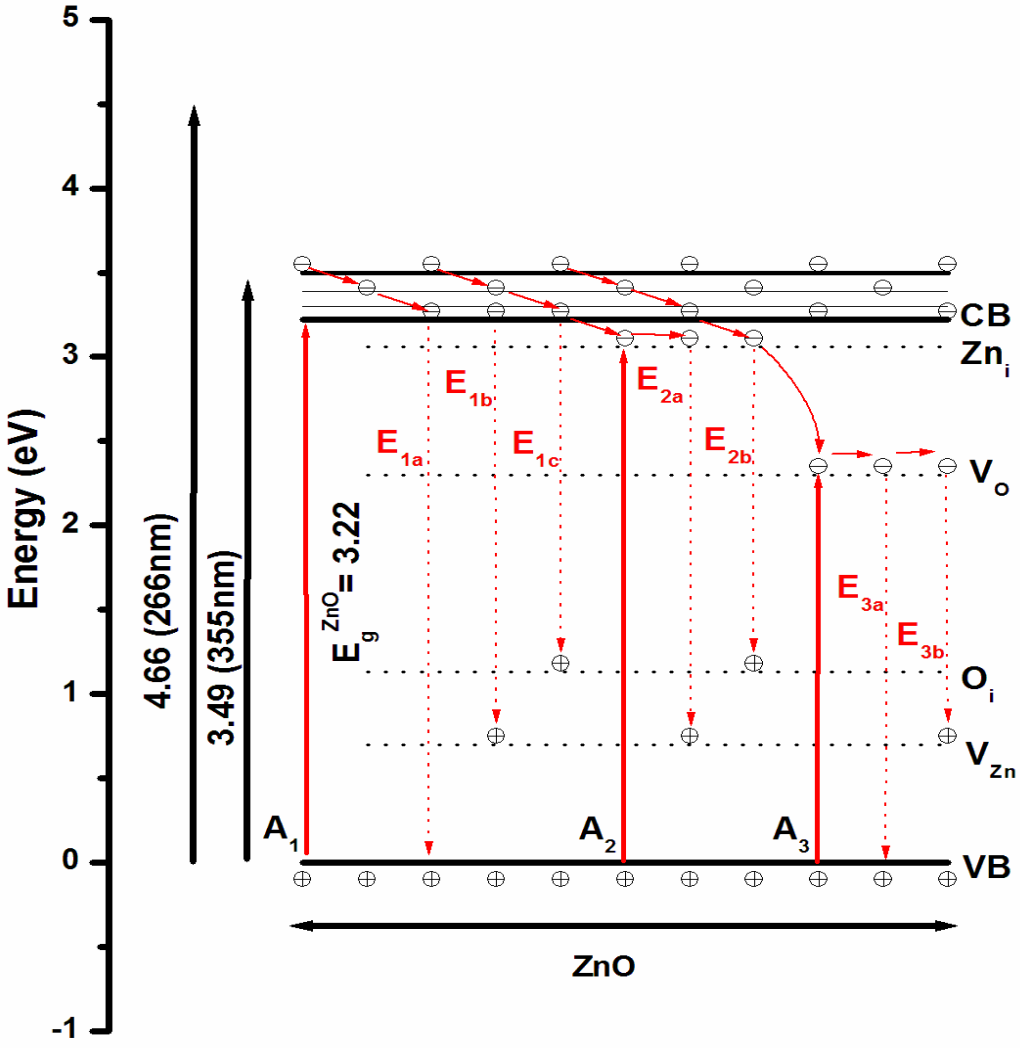

Figure 4.27: The proposed energy band diagram of the electron transfer in ZnO after excitation**.**

4.4 Conclusions

ZnO powders synthesised through different techniques such as coprecipitation, sol-gel and solution combustion were calcined at different temperatures. Defects in ZnO were observed from strain in the lattice and confirmed from various spectroscopic techniques such as Raman, photoluminescence and positron annihilation spectroscopy. The morphologies of the samples were observed through FE-SEM. ZnO powder samples prepared through coprecipitation method showed varying morphology from 2D plates to triangular as well as hexagonal rods, needles and finally to hierarchical structures just by varying the *p*H from 5.5 to 13. In addition, the impurity phases of $Zn_5(OH)_8(NO_3)_2(H_2O)_2$ or ε-$Zn(OH)_2$ were observed for lowest *p*H (5.5 and 7) and highest *p*H (11.5 and 13) samples, respectively. Pure wurtzite ZnO was observed in the samples synthesised at *p*H in between 9 to 10. It was observed that the intermediate phase of $Zn_5(OH)_8(NO_3)_2(H_2O)_2$ or ε-$Zn(OH)_2$ were responsible for the systematic growth of ZnO crystals. A mechanism for crystal growth for the samples synthesised through coprecipitation technique, by varying the *p*H, was proposed. On the other hand, these impurity phases also acted like intermediate phases that decomposed into ZnO after drying at 250 ^oC. PL study revealed the NBE and DBE emission, where DBE band appeared due to native defects. These defects increased with increase in *p*H of precipitation and were suppressed after drying at 250 ^oC as confirmed by PAS.

ZnO samples synthesised through sol-gel and combustion techniques and calcined at four different temperatures. W-H plot shows the decreasing slope in sol-gel samples with increasing calcination temperature. While the slope was positive indicating tensile strain in the lattice upto calcination temperature, 800 ^oC and approached to zero for the sample calcined at 1000 ^oC calcination temperature. In contrary to sol-gel, negative slope was found in combustion synthesised samples which correspond to compressive strain. The strain in ZnO sample is often reported due the native defects. In Raman measurement, we observed that the intensity of $E_1(LO)$ mode which is a Raman active mode enhanced anomalously in both the samples. With increasing

calcination temperature, the intensity of the $E_1(LO)$ mode were decreased in both the cases. Further, while PL spectra showed no DBE peak in samples synthesised through sol-gel, it was found to increase with increase in calcination temperature in case of combustion synthesised samples. Although $E_1(LO)$ mode varied in similar fashion in both the cases, the behaviour of DBE peak clearly indicated different native defects in both cases. In literature the anomalous nature of $E_1(LO)$ mode is reported due to native defects, specially Zn_i and the increase in DBE could be due to O_i. PAS confirmed the presence of native defects in both cases by showing the cluster of (Zn+O) divacancies.